

# Distorted, nonspherical transiting planets: impact on the transit depth and on the radius determination<sup>★</sup>

J. Leconte<sup>1,2,3,6</sup>, D. Lai<sup>4,6</sup>, and G. Chabrier<sup>1,2,3,5,6</sup>

<sup>1</sup> École Normale Supérieure de Lyon, 46 allée d'Italie, 69364 Lyon Cedex 07, France  
e-mail: [jeremy.leconte;chabrier]@ens-lyon.fr

<sup>2</sup> Université Lyon 1, 69622 Villeurbanne, France

<sup>3</sup> CNRS, UMR 5574, Centre de Recherche Astrophysique de Lyon, France

<sup>4</sup> Center for Space Research, Department of Astronomy, Cornell University, Ithaca, NY 14853, USA

<sup>5</sup> School of Physics, University of Exeter, Exeter, UK

<sup>6</sup> KITP, University of California Santa Barbara, Kohn hall, CA 93106-4030, USA

Received 23 September 2010 / Accepted 14 January 2011

## ABSTRACT

In this paper, we quantify the systematic impact of the nonspherical shape of transiting planets caused by tidal forces and rotation on the observed transit depth. Such a departure from sphericity leads to a bias in the derivation of the transit radius from the light curve and affects the comparison with planet structure and evolution models, which assume spherical symmetry. As the tidally deformed planet projects its smallest cross section area during the transit, the measured effective radius is smaller than the one of the unperturbed spherical planet (which is the radius predicted by 1D evolution models). This effect can be corrected by calculating the theoretical *shape* of the observed planet.

Using a variational method and a simple polytropic assumption for the gaseous planet structure, we derived simple *analytical* expressions for the ellipsoidal shape of a fluid object (star or planet) accounting for both tidal and rotational deformations. We determined the characteristic polytropic indexes that describe the structures of irradiated close-in planets within the mass range  $0.3 M_J < M_p < 75 M_J$ , at different ages, by comparing polytropic models with the inner density profiles calculated with the full evolution code. Our calculations yield a 20% effect on the transit depth, i.e. a 10% decrease in the measured radius, for the extreme case of a  $1 M_J$  planet orbiting a Sun-like star at 0.01 AU, and the effect can be greater for lower mass objects. For the closest planets detected so far ( $\leq 0.05$  AU), the effect on the radius is of the order of 1 to 10%, by no means a negligible effect, enhancing the puzzling problem of the anomalously large bloated planets. These corrections must thus be taken into account for correctly determining the radius from the transit light curve and when comparing theoretical models with observations.

Our analytical expressions can be easily used to calculate these corrections, caused by the nonspherical shape of the planet, on the observed transit depth and thus to derive the planet's real equilibrium radius, the one to be used when comparing models with observations. They can also be used to model ellipsoidal variations in the stellar flux now detected in the CoRoT and Kepler light curves. We also derive directly usable analytical expressions for the moment of inertia and the Love number ( $k_2$ ) of a fluid planet as a function of its mass and, in the case of significant rotation, for its oblateness.

**Key words.** planets and satellites: general – planets and satellites: interiors – planets and satellites: fundamental parameters – equation of state

## 1. Introduction

Because the measurement of the radii of close-in transiting planets continues to gain in accuracy, providing stringent constraints on exoplanet theoretical models, any source of errors in the radius determination must be determined with precision. Current ground and space-based photometric observations of the host stars of transiting planets enable us to address new problems. The first direct detection with Spitzer of the light emitted by the planet (Deming et al. 2007) opened a new path for probing the physical properties of the surface and the atmosphere of transiting exoplanets. Among the first results of the *Kepler* mission, the detection of ellipsoidal variations of the host star induced by tidal interaction with a low mass companion has been claimed Welsh et al. (2010). More recently, Carter & Winn (2010a,b)

have shown that light curve analysis can put direct constraints on the actual shape of transiting planets. They also investigated the impact of the precession of an oblate object with a non zero obliquity around the orbital axis on the shape and timing of the transit signal.

These observations motivate us to investigate the deformation of the planet with respect to a spherical body and caused by tidal or rotational forces. While previous studies have focused on the detectability of the oblateness of a flattened body, we address the more general problem in the present paper, namely the determination of the *general shape* of a planet (or star) distorted by both a tidal and a centrifugal potential, and its impact on the transit depth, hence on the determination of its correct radius. In order to compute the ellipsoidal shape (flattening and triaxiality) of a gaseous body, we derive in Sect. 2 a simple analytical model of the internal structure of the object based on the polytropic equation of state (Lai et al. 1994). The polytropic indexes are calibrated in Sect. 4 by comparing with numerical models

<sup>★</sup> Tables B.2 and B.3 are only available in electronic form at <http://www.aanda.org>

describing the structure of strongly irradiated gaseous planets (Leconte et al. 2009). In Sect. 3, we present directly usable analytical expressions giving the shape (oblateness and triaxiality) of a distorted planet (or star) as a function of its mass and polytropic index and compare our estimates with the numerical method outlined in Appendix A and with the measured values for the major planets of our solar system. As a by-product, our model yields analytical expression for the first gravitational moment  $J_2$  and the love number  $k_2$  of a self gravitating fluid body. Finally, Sect. 5 quantifies the effect of the non-sphericity of the planet on the transit depth.

We find that as the planet transits across the stellar disc, we only see the smallest cross section of its actual ellipsoidal shape so that the depth of the transit is *decreased* with respect to the expected signal for a spherical object, as discussed by Li et al. (2010) in the case of WASP-12 b. This implies that the radius inferred from the light curve analysis, derived under the assumption of spherical planet and star, *underestimates* the real equilibrium radius of the object. This bias needs to be corrected for a proper comparison of the structure and evolution of extrasolar planets with theoretical 1D numerical simulations and enhances the actual discrepancy between theory and observation for the so-called “bloated” planets.

## 2. Variational method for compressible ellipsoids

In this section, we briefly describe the energy variational method developed by Lai et al. (1993) and Lai et al. (1994) (hereafter LRS1 and LRS2) to construct general Darwin-Riemann equilibrium models. In Sect. 2.1 we briefly summarize the basic assumptions and the equilibrium relations are derived in Sect. 2.2. More details about the method in general, as well as the applications to compact objects, can be found in LRS1 and LRS2, and references to equations in these papers are denoted with numbers preceded by “I” and “II”, respectively, in the present paper. Solutions to first order in the deformation are derived for tidal and rotational deformations in Sects. 3.2 and 3.1, respectively.

### 2.1. Model description

Consider an isolated, self-gravitating fluid system in steady state. The system is characterized by conserved global quantities such as its total mass  $M$  and total angular momentum  $J$ . The basic idea in our method is to model our self gravitating system by a limited number of parameters  $x_1, x_2, \dots$  and in such a way that the total energy can be written as

$$E = E(x_1, x_2, \dots; M, J, \dots). \quad (1)$$

An equilibrium configuration is then determined by extremizing the energy according to

$$\left. \frac{\partial E}{\partial x_i} \right|_{M, J, \dots} = 0, \quad i = 1, 2, \dots \quad (2)$$

An expression like Eq. (1) can be written down for the total energy of a binary system (with components of mass  $M$  and  $M'$ ). We adopt a polytropic equation of state between the pressure  $P$  and the mass density  $\rho$ ,

$$P = K\rho^{1+1/n}. \quad (3)$$

This defines the polytropic index  $n$  and the “entropy”  $K$  – both are constant within the object and sufficient (with  $M$ ) to describe the mechanical structure of a given object. Under the combined

effects of centrifugal and tidal forces, the objects (stars or planets) achieve nonspherical shapes. We model these shapes as triaxial ellipsoids of principal axes  $(a_1, a_2, a_3)$  and  $(a'_1, a'_2, a'_3)$ , respectively. Throughout this paper, unprimed quantities refer to the component of mass  $M$  while primed quantities refer to the component of mass  $M'$ . The three directions along which our principal axes are measured are, respectively, the line connecting the center of mass of the two components, its normal contained in the orbital plane, and the direction of the orbital angular momentum vector. In the simple case of coplanar and synchronous rotation,  $a_3$  is simply the polar radius and  $a_1$  and  $a_2$  are the equatorial radii of the component measured toward its companion and in the orthogonal direction, respectively.

Specifically, we assume that the surfaces of constant density within each object can be modeled as *self-similar ellipsoids*. The geometry is then completely specified by the three principle axes of the outer surface. Furthermore, we assume that the density profile  $\rho(m)$  inside each component, where  $m$  is the mass interior to an isodensity surface, is identical to that of a *spherical* polytrope with the same volume. The velocity field,  $\mathbf{v}$ , of the fluid is modeled as either uniform rotation (corresponding to the case of a synchronized binary system) or uniform *vorticity*,  $\nabla \times \mathbf{v}$ , (for nonsynchronized systems). The vorticity vector is assumed to be parallel everywhere to the orbital rotation axis.

For an isolated rotating gaseous sphere, these assumptions are satisfied *exactly* when the fluid is incompressible (polytropic index  $n = 0$ ), in which case the true equilibrium configuration is a homogeneous ellipsoid (Chandrasekhar 1969). For a binary system, our assumptions are strictly valid in the incompressible limit only if we truncate the tidal interaction at the quadrupole order. We adopt this quadrupole-order truncation of the interaction potential in this paper.

After adding up the orbital separation,  $r$ , our set of unknowns is  $(r, a_1, a_2, a_3, a'_1, a'_2, a'_3)$  or equivalently  $(r, \rho_c, \lambda_1, \lambda_2, \rho'_c, \lambda'_1, \lambda'_2)$  where  $\rho_c$  is the central density and  $\lambda_1 \equiv (a_3/a_1)^{2/3}$ ,  $\lambda_2 \equiv (a_3/a_2)^{2/3}$  (when no ambiguity exists or otherwise stated, primed quantities are defined in the same manner as unprimed ones by simply making the transformation  $x \rightleftharpoons x'$  throughout the equations). The total energy can be written

$$E = U + U' + W + W' + T + W_i, \quad (4)$$

where

$$U = \int \frac{nP}{\rho} dm = \bar{k}_1 K \rho_c^{1/n} M \quad (5)$$

is the internal energy of component 1 (cf. Eq. (I.3.1)), and

$$W = -\frac{3}{5-n} \frac{GM^2}{R} \bar{f} = -\bar{k}_2 GM^{5/3} \rho_c^{1/3} \bar{f} \quad (6)$$

is the self-gravitational energy of component 1 (cf. Eq. (I.4.6)) with,

$$\bar{k}_1 \equiv \frac{n(n+1)}{5-n} \xi_1 \left| \frac{d\theta}{d\xi} \right|_{\xi_1}, \quad (7)$$

$$\bar{k}_2 \equiv \frac{3}{5-n} \left( \frac{4\pi}{\xi_1} \left| \frac{d\theta}{d\xi} \right|_{\xi_1} \right)^{1/3}, \quad (8)$$

$$\bar{f}(\lambda_1, \lambda_2) \equiv \frac{A_1 a_1^2 + A_2 a_2^2 + A_3 a_3^2}{2(a_1 a_2 a_3)^{2/3}}, \quad (9)$$

$$A_i \equiv a_1 a_2 a_3 \int_0^\infty \frac{du}{\Pi(a_i^2 + u)}, \quad (10)$$

and

$$\Pi^2 \equiv (a_1^2 + u)(a_2^2 + u)(a_3^2 + u).$$

The dimensionless radius and density,  $\xi$  and  $\theta$  (with a subscript 1 when taken at the surface), are the classical variables used to describe polytropic gaseous spheres (see [Chandrasekhar 1939](#)) and  $G$  is the gravitational constant. The kinetic energy in the inertial frame reads

$$T = T_s + T'_s + T_0 \quad (11)$$

where the spin kinetic energy of body 1 ( $T_s$ ) is given by (cf. Eq. (I.5.6))

$$T_s = \frac{1}{2}I(\Lambda^2 + \Omega^2) - \frac{2}{5}\kappa_n Ma_1 a_2 \Lambda \Omega, \quad (12)$$

with  $\Omega$  being the rotational orbital velocity,  $\Lambda$  is a measure of the internal rotation rate in the co-rotating frame,

$$\kappa_n \equiv \frac{5}{3} \frac{\int_0^{\xi_1} \theta^n \xi^4 d\xi}{\xi_1^4 \left| \frac{d\theta}{d\xi} \right|_{\xi_1}} \quad (13)$$

is a dimensionless coefficient measuring the inertia of the body, and

$$I = \frac{1}{5}\kappa_n M(a_1^2 + a_2^2) \quad (14)$$

is the moment of inertia with respect to the rotation axis. Tables giving values of the polytropic constants  $\bar{k}_1$ ,  $\bar{k}_2$ ,  $\kappa_n$ ,  $\theta'_1$  and  $\xi_1$  as a function of  $n$  can be found in LRS1 and in [Chandrasekhar \(1939\)](#). For non synchronous rotation ( $\Lambda \neq 0$ ), our gaseous body is not in the state of solid-body rotation. A rotation rate can thus not have the usual meaning. To have a sense of the angular velocity, one can take the half of the vorticity ( $\omega = \frac{\nabla \times \mathbf{v}}{2}$ , where  $\mathbf{v}$  is the fluid velocity vector in the inertial frame) as a proxy<sup>1</sup>.  $\omega$  is related to  $\Lambda$  by

$$\omega = \Omega - \frac{a_1^2 + a_2^2}{2a_1 a_2} \Lambda. \quad (15)$$

The orbital kinetic energy  $T_0$  is simply

$$T_0 = \frac{1}{2} \frac{MM'}{M + M'} \Omega^2 r^2. \quad (16)$$

Finally, the gravitational interaction energy  $W_i$  reads

$$W_i = -\frac{GMM'}{r} - \frac{GM}{2r^3}(2I'_{11} - I'_{22} - I'_{33}) - \frac{GM'}{2r^3}(2I_{11} - I_{22} - I_{33}), \quad (17)$$

with

$$I_{ij} = \frac{1}{5}\kappa_n M a_1^2 \delta_{ij}. \quad (18)$$

<sup>1</sup> This choice has no impact on the result to first order because i) there is no cross correlation between tidal and centrifugal distortion at this level and ii) the value of  $\omega$  only plays a role to compute the rotational distortion for which solid body rotation is ensured because  $a_1 = a_2$ . In this case, the half vorticity reduces to the usual rotation rate and  $\omega = \Omega - \Lambda$ . To higher order, this simply highlights the absence of a solidly rotating state and the inadequacy of the parametrization by a rotation rate in such cases.

## 2.2. Equilibrium relations

We can now derive the set of equilibrium relations

$$\left\{ \frac{\partial E}{\partial x_i} \Big|_{M,J,\dots} = 0 \right\}_{i=1,\dots,7}$$

yielding seven algebraic equations for our seven unknowns ( $r, \rho_c, \lambda_1, \lambda_2, \rho'_c, \lambda'_1, \lambda'_2$ ). The details of the transformations necessary to express the total energy as a function of the unknowns and conserved quantities alone and to be able to carry out the differentiation are explained in Sect. 2.2.1 of LRS2 and just add technical details not needed here. We thus give only the results. Differentiation with respect to  $r$  simply yields the modified Kepler's law for the orbital mean motion  $\Omega$

$$\Omega^2 = \frac{G(M + M')}{r^3} (1 + \Delta + \Delta'), \quad (19)$$

with

$$\Delta \equiv \frac{3}{2} \frac{(2I_{11} - I_{22} - I_{33})}{Mr^2}. \quad (20)$$

Differentiation with respect to the central density  $\rho_c$  yields the *virial relation*,

$$\frac{3}{n}U + W + 2T_s = -\frac{GMM'}{R}g_t \quad (21)$$

with the mean radius  $R = (a_1 a_2 a_3)^{1/3}$  and

$$g_t \equiv \frac{R}{Mr^3} (2I_{11} - I_{22} - I_{33}) = \frac{2}{3} \frac{R}{r} \Delta. \quad (22)$$

Using expressions for  $U$  and  $W$ , we get the equilibrium mean radius

$$R = R_0 \left[ \bar{f}(\lambda_1, \lambda_2) \left( 1 - 2 \frac{T_s}{|W|} \right) - \left( \frac{5-n}{3} \right) \frac{M'}{M} g_t \right]^{\frac{n}{n-3}}, \quad (23)$$

where  $R_0$  is the radius of the *unperturbed* spherical polytrope given by ([Chandrasekhar 1939](#))

$$R_0 = \xi_1 \left( \xi_1^2 \left| \frac{d\theta}{d\xi} \right|_{\xi_1} \right)^{\frac{n-1}{3-n}} \left[ \frac{(n+1)K}{4\pi G} \right]^{\frac{n}{3-n}} \left( \frac{M}{4\pi} \right)^{\frac{1-n}{3-n}}. \quad (24)$$

Finally, the differentiation with respect to  $\lambda_1$  and  $\lambda_2$  yields after some algebra (cf. Eqs. (I.8.4)–(I.8.6)):

$$\left\{ \left[ 2 + \frac{\Omega^2}{\mu_R} - 2 \frac{a_2 \Lambda \Omega}{a_1 \mu_R} + \frac{\Lambda^2}{\mu_R} \right] a_1^2 + a_3^2 \right\} = \frac{2}{q_n \tilde{\mu}_R} (a_1^2 A_1 - a_3^2 A_3), \quad (25)$$

$$\left\{ \left[ \frac{\Omega^2}{\mu_R} - 1 - \frac{2a_1 \Lambda \Omega}{a_2 \mu_R} + \frac{\Lambda^2}{\mu_R} \right] a_2^2 + a_3^2 \right\} = \frac{2}{q_n \tilde{\mu}_R} (a_2^2 A_2 - a_3^2 A_3), \quad (26)$$

where

$$q_n \equiv \kappa_n \left( 1 - \frac{n}{5} \right),$$

$\mu_R \equiv GM'/r^3$ ,  $\tilde{\mu}_R \equiv \mu_R/(\pi G \bar{\rho})$ , and  $\bar{\rho} \equiv M/(\frac{4}{3}\pi R^3)$  is the mean density of the ellipsoid.

### 3. The shape of gaseous bodies

In this section, we derive analytical expressions for the deformation – induced either by centrifugal or tidal potential – of a gaseous body. To test the validity of our assumptions, we compared our predictions with the measured values for the major planets of our solar system in Sect. 3.1. Since we do not make any assumption about the masses of the two components, these equations can be used indifferently to compute the shape of the star or of the planet by choosing  $M = M_p$  and  $M' = M_\star$  when considering the planet, and vice versa when focusing on the star.

In general, the set of equations described in the previous section must be solved numerically, but we study here the first order development of these equations at large orbital separation. This approximation corresponds to neglecting terms of order  $O(R_0^5/r^5)$ , which is consistent with our truncation of the gravitational potential at the quadrupole order and is appropriate to address close-in transiting planetary systems. In practice, this is done by setting  $\Delta = \Delta' = 0$  and

$$a_i \equiv R_0(1 + \alpha_i), \quad (27)$$

in Eqs. (19), (23), (25), (26) and their primed equivalent and by expanding these equations to first order in  $\alpha_i$  ( $O(R_0^3/r^3)$ ). First we derive some general formulae by expanding the integrand in the definition (10):

$$A_i = R_0^3(1 + \alpha_1 + \alpha_2 + \alpha_3) \times \int_0^\infty \left[ 1 - \frac{R_0^2}{R_0^2 + u}(\alpha_1 + \alpha_2 + \alpha_3 + 2\alpha_i) \right] \frac{du}{(R_0^2 + u)^{5/2}},$$

which yields

$$A_i = \frac{2}{3} + \frac{4}{15}(\alpha_1 + \alpha_2 + \alpha_3) - \frac{4}{5}\alpha_i + O(\alpha_i^2).$$

To first order,

$$\bar{f}(\lambda_1, \lambda_2) = 1 + O(\alpha_i^2), \quad (28)$$

and

$$A_1 a_1^2 - A_3 a_3^2 = \frac{8}{15}(\alpha_1 - \alpha_3)R_0^2, \\ A_2 a_2^2 - A_3 a_3^2 = \frac{8}{15}(\alpha_2 - \alpha_3)R_0^2. \quad (29)$$

The principal moment of inertia of the body can also be computed and reads

$$I = \frac{1}{5}\kappa_n M(a_1^2 + a_2^2) \\ \approx \frac{2}{5}\kappa_n M R_0^2 (1 + \alpha_1 + \alpha_2) \\ = \frac{2}{5}\kappa_n M R_0^2 \text{ (spherical case)}. \quad (30)$$

The other moments of inertia can be computed by replacing 1 and 2 by the appropriate indices. The dimensionless moment of inertia  $\kappa_n$  for different planetary masses, age and stellar irradiation can be found in Tables B.2 and B.3.

#### 3.1. Rotational deformation: Maclaurin spheroids

Our set of equations also allows us to compute the effect of the centrifugal force alone on a slowly rotating fluid object. To do so, one just has to take the  $M' \rightarrow 0$  limit in Eqs. (19), (23), (25) and (26). Therefore,  $\Omega$  is a free parameter (the rotation rate of our body) and there is a degeneracy between  $\Omega$  and  $\Lambda$  that allows us to choose  $\Lambda = 0$ .

We introduce the dimensionless angular velocity

$$\bar{\omega}^2 \equiv \frac{\omega^2 R_0^3}{GM} \quad (31)$$

as a small parameter of order  $O(\alpha_i)$  in all expansions. The volume expansion factor can be calculated using

$$\frac{T_s}{|W|} = \frac{\frac{1}{2}I\omega^2}{\frac{3}{5-n} \frac{GM^2}{R}} = \frac{1}{3}q_n \bar{\omega}^2. \quad (32)$$

We get

$$\frac{a_1 a_2 a_3}{R_0^3} - 1 = \alpha_1 + \alpha_2 + \alpha_3 = \frac{2n}{3-n} q_n \bar{\omega}^2. \quad (33)$$

To the same order of approximation, the two remaining equations are given by Eqs. (25) and (26) which yield

$$q_n \bar{\omega}^2 = \frac{4}{5}(\alpha_{1,2} - \alpha_3). \quad (34)$$

Combinations of Eqs. (33) and (34) give the three figure functions (cf. Eq. (A12) of LRS2)

$$\alpha_1 = \alpha_2 = \frac{1}{4} \frac{5+n}{3-n} q_n \bar{\omega}^2 \\ \alpha_3 = -\frac{1}{2} \frac{5-3n}{3-n} q_n \bar{\omega}^2. \quad (35)$$

For this configuration, the usual variables are the oblateness

$$f = \frac{a_1 - a_3}{a_1} = \alpha_1 - \alpha_3 = \frac{5}{4} q_n \bar{\omega}^2, \quad (36)$$

and the dimensionless quadrupole moment of the gravitational field  $J_2$  given by the theory of figures to first order (Zharkov et al. 1973)

$$J_2 = \frac{2}{3}f - \frac{\bar{\omega}^2}{3} = \frac{5q_n - 2}{6} \frac{\omega^2 R_0^3}{GM}. \quad (37)$$

For practical purposes,  $R_0$  can be computed to first order by using Eq. (27) and reads

$$R_0 = \sqrt{3 \frac{a_1 a_2 a_3}{a_1 + a_2 + a_3}} = \sqrt{\frac{3 R_{\text{eq}}^2 R_{\text{pol}}}{2 R_{\text{eq}} + R_{\text{pol}}}}, \quad (38)$$

in our geometry, where  $R_{\text{eq}}$  and  $R_{\text{pol}}$  denote the usual equatorial and polar radii. For an incompressible body ( $n = 0$ ) we retrieve the usual solution of the theory of planetary figures  $f = 5/4 \bar{\omega}^2$  (Zharkov & Trubitsyn 1980).

Attempts have been made to constrain the oblateness and thus the rotation period of transiting planets by using the solar system planets as test cases (Carter & Winn 2010a,b). Because of the wide variety of exoplanets, it is important to have the ability to predict the flattening of fluid planets for a wider range of parameters than encountered in the solar system. Figure 1 shows the predicted oblateness for various planet masses as a function of the rotational period  $P_{\text{rot}} = \frac{2\pi}{\omega}$ .

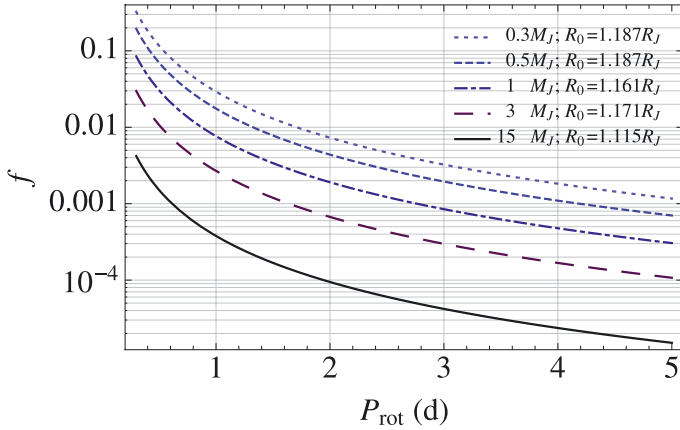


**Fig. 1.** Oblateness given by Eq. (36) as a function of the rotation period (in days) at 1 Gyr for planets of mass:  $0.3 M_J$  (dotted),  $0.5 M_J$  (dashed),  $1 M_J$  (dash-dotted),  $3 M_J$  (long dashed),  $15 M_J$  (solid). The oblateness decreases when the mass of the planet increases because massive objects are more compressible (see Sect. 4), have a more intense self-gravity field and are thus less subject to perturbations.

### 3.2. Tidal deformation: determination of the Love number ( $k_2$ )

To compute the shape induced by the tidal force alone, we consider a non-rotating configuration ( $\omega = 0$ ). From Eq. (15), this is achieved if  $\Lambda = 2a_1a_2\Omega/(a_1^2 + a_2^2)$ . Then

$$\begin{aligned} T_s &= \frac{1}{2}I\Omega^2 \left( 1 - \left( \frac{2a_1a_2}{a_1^2 + a_2^2} \right)^2 \right) \\ &= -I\Omega^2\alpha_1\alpha_2 = 0 + O(\alpha_i^2). \end{aligned}$$

Thus from Eq. (23) we see that there is no change of volume to lowest order,

$$\frac{a_1a_2a_3}{R_0^3} - 1 = 0.$$

Since  $\Omega^2 = \mu_R(1+p)$  with  $p = M/M'$  and  $\tilde{\mu}_R = O(R_0^3/r^3)$ , only the zeroth order must be taken in the left hand side of Eqs. (25) and (26), which yields (with help of Eq. (29))

$$\begin{aligned} \alpha_1 - \alpha_3 &= \frac{15}{4}q_n \frac{1}{p} \frac{R_0^3}{r^3}, \\ \alpha_2 - \alpha_3 &= 0. \end{aligned} \quad (39)$$

Thus (cf. Eq. (A25) of LRS2)

$$\begin{aligned} \alpha_1 &= \frac{5}{2}q_n \frac{1}{p} \frac{R_0^3}{r^3}, \\ \alpha_2 = \alpha_3 &= -\frac{5}{4}q_n \frac{1}{p} \frac{R_0^3}{r^3}. \end{aligned} \quad (40)$$

As long as the hydrostatic equilibrium holds, *this equation can be used to compute the shape of the planet and its host star at each point of the orbit.* We recover the usual dependence of the tidal deformation in  $\frac{M'R_0^3}{Mr^3}$ , with a factor of order unity,  $q_n$ , which encompasses all the structural properties of the gaseous configuration.

Since we are in the linear approximation with a gravitational potential restricted to quadrupolar order, the shape of our body can be described with the usual Love number of second order,

$k_2$  (Love 1909, which is twice the apsidal motion constant often called  $k_2$  in the stellar binary literature). Indeed, once  $k_2$  (and  $h_2 = 1 + k_2$  for a body in hydrostatic equilibrium) is known, the external potential and the shape that a body will exhibit in response to any perturbing potential can be computed as detailed in Appendix A. To derive  $k_2$ , we compute the quadrupolar term of the gravitational potential energy of the system formed by our compressible ellipsoid and a point mass, by introducing Eq. (40) in the linearized version of Eq. (17), and identify this term to the potential energy due to tides given by (Darwin 1908)

$$W_{\text{tides}} = -k_2 \frac{GMM'R_0^5}{r^6}. \quad (41)$$

This yields

$$\begin{aligned} k_2 &= \frac{3}{2} \frac{q_n^2}{1 - \frac{n}{5}} \\ &= \frac{3}{2} \kappa_n^2 \left( 1 - \frac{n}{5} \right). \end{aligned} \quad (42)$$

As expected, in the  $n = 0$  limit, we retrieve the Love number of an incompressible ideal fluid planet  $k_2 = 3/2$ . We can also see that  $k_2$  is linked to the square of the dimensionless moment of inertia  $\kappa_n$ . This is because level surfaces are self-similar in our model and that the love number encompass both the deformation of the body ( $\propto \kappa_n$ ) and the gravitational potential created by the deformation ( $\propto \kappa_n$ ). The Love number for different planetary masses, age and stellar irradiation can be found in Tables B.2 and B.3.

We can see that the value of the Love number tends to decrease with mass above  $1 M_J$ . This is due to the fact that more massive objects are more compressible and thus more centrally condensed (see Sect. 4). At constant mass, enrichment in heavy elements toward the center (possibly in a core) acts to decrease the value of  $k_2$ . In general, redistributing mass from the external to the internal layers, which are less sensitive to the disturbing potential, decreases the response of the body to an exciting potential, which translates into a lower  $k_2$ .

Our model predicts  $k_2$  values in the range 0.3–0.6. As discussed by Ragozzine & Wolf (2009) such values of the Love number could be inferred by the measurement of the precession rate of very Hot Jupiters on eccentric orbits. Such measurements could be carried out by *Kepler* for WASP-12 b analogs with an eccentricity  $> 3 \times 10^{-4}$  (most favorable case) or *Tres-3 b* analogs with an eccentricity  $> 2 \times 10^{-3}$  (for  $k_2 \approx 0.3$ ) and lower eccentricities for higher Love number values. Such measurements would indeed be extremely valuable as they would put direct constraints on the central enrichment in heavy elements inside close Hot Jupiters, like the measurements of the gravitational moments of the solar system planets.

### 3.3. Synchronized planets

For values of the tidal dissipation factors inferred for Jupiter (Goldreich & Soter 1966; Leconte et al. 2010), the timescale of pseudo synchronization of close-in giant planets is less than about a million years. The planet is thus in a state of pseudo synchronization, with a rotation rate given by (Hut 1981; Leconte et al. 2010)

$$\omega_p = \frac{1 + \frac{15}{2}e^2 + \frac{45}{8}e^4 + \frac{5}{16}e^6}{\left(1 + 3e^2 + \frac{3}{8}e^4\right)(1 - e^2)^{3/2}} \Omega \quad (43)$$

in the weak friction theory, with  $e$  being the eccentricity of the orbit. For the simple case of a circular orbit, the spin is thus synchronized and, either solving Eqs. (19), (23), (25) and (26) in the synchronized case ( $\Lambda = 0$ ) or simply adding the results of Eqs. (40) and (35) (there is no cross correlation terms to first order) yields

$$\begin{aligned} \alpha_1 &= \frac{1}{3}q_n \left( \frac{1+p}{p} \right) \frac{R_0^3}{r^3} \left[ \frac{5}{4} \left( \frac{7+p}{1+p} \right) + \left( \frac{2n}{3-n} \right) \right] \\ \alpha_2 &= -\frac{1}{3}q_n \left( \frac{1+p}{p} \right) \frac{R_0^3}{r^3} \left[ \frac{5}{4} \left( \frac{2-p}{1+p} \right) - \left( \frac{2n}{3-n} \right) \right] \\ \alpha_3 &= -\frac{1}{3}q_n \left( \frac{1+p}{p} \right) \frac{R_0^3}{r^3} \left[ \frac{5}{4} \left( \frac{5+2p}{1+p} \right) - \left( \frac{2n}{3-n} \right) \right], \end{aligned} \quad (44)$$

and

$$\frac{R^3}{R_0^3} = 1 + q_n \left( \frac{2n}{3-n} \right) \left( \frac{1+p}{p} \right) \frac{R_0^3}{r^3}. \quad (45)$$

### 3.4. Model validation

There are two major assumptions in the present calculations:

- the absence of a central core. The aim of such an approximation is to avoid to introduce any free parameter in the model. In any case, the core mass and the global enrichment in giant extrasolar planets are yet weakly constrained (Guillot 2005; Leconte et al. 2009). We show that this approximation introduces an uncertainty of  $\approx 10\%$  on the derived shape;
- the polytropic assumption. This allows us to derive a *completely analytical model*. Comparison with a more detailed numerical integration (see Appendix A) shows that the deviation between the results of the two models (analytical vs. numerical) is smaller than the uncertainty due to the no-core approximation.

Since the oblateness ( $f$ ),  $J_2$ ,  $k_2$ , the mean radius and rotation rate are known for the major planets of our solar system, we can test our theory on these objects. The details of the calculation of the chosen polytropic indexes are presented in Sect. 4. The results are summarized in Table 1, which shows the actual values of the relevant parameters for the two major planets taken from Guillot (2005), the values of the oblateness and of  $J_2$  calculated with our model and, for comparison, with the assumption of an incompressible body ( $n = 0$ ). We see that, whereas the values of  $f$  derived from the incompressible model differ from the true values by almost a factor of 2, our polytropic model predicts the  $f$ -values to within 12%. Note that higher-order terms (of order  $\bar{\omega}^2 \sim 10\%$ ) are not completely negligible for rapidly rotating bodies such as Jupiter and Saturn (see Zharkov et al. 1973; Chabrier et al. 1992). The polytropic model, however, yields  $J_2$ -values that differ from the measured values by 30% (for Jupiter) and 59% (for Saturn). These discrepancies are mostly due to the large metal enrichment in these planet interiors, probably with the presence of a large dense core as detailed three layers models can reproduce exactly the measured moments (Chabrier et al. 1992). Note that this no-core approximation has less relative impact on the distortion of the shape predicted by the model than on the gravitational moments because these effects scale as  $h_2 = 1 + k_2$  (see Appendix A) and  $k_2$  respectively,  $k_2$  being  $\leq 0.6$  in the situations of interest. Such discontinuities in the density profile (and its derivatives) could be addressed more precisely

**Table 1.** Comparison between the measured oblateness and data of the gravity fields and the values obtained with our polytropic model (polytrope) and with a model with  $n = 0$  (incompressible).

	Jupiter	Saturn
$M_p$ [ $10^{26}$ kg]	18.986112(15)	5.684640(30)
$R_{\text{eq}}$ [ $10^7$ m]	7.1492(4)	6.0268(4)
$R_{\text{pol}}$ [ $10^7$ m]	6.6854(10)	5.4364(10)
$R_0$ [ $10^7$ m]	6.9894	5.8198
$P_{\text{rot}}$ [ $10^4$ s]	3.57297(41)	3.83577(47)
$\bar{\omega}^2 \times 10^2$	8.332	13.940
$k_2$	0.49	0.32
$n$	0.936	0.748
$q_n$	0.547	0.623
$f \times 10^2$	6.487(8)	9.796(9)
$f \times 10^2$ (polytrope)	5.701	10.849
$f \times 10^2$ (incompressible)	10.416	17.425
$J_2 \times 10^2$	1.4697(1)	1.6332(10)
$J_2 \times 10^2$ (polytrope)	1.023	2.586
$J_2 \times 10^2$ (incompressible)	4.166	6.970

**Notes.** The numbers in parentheses are the uncertainty in the last digits of the value.

with two different polytropes, but this would add extra free parameters and would not serve the actual purpose of the present paper.

While we decided to use a polytropic assumption to infer a fully analytical theory, the figures of a body in hydrostatic equilibrium can be derived without this assumption. As shown in Sterne (1939) (see also Zharkov et al. 1973; Zharkov & Trubitsyn 1980; Chabrier et al. 1992, for more detailed applications to the giant planets case) and outlined in Appendix A, this theory, however, requires a numerical integration even to first order. For an ideal  $n = 1$  polytropic sphere, Eq. (42) agrees with the numerical results of Sterne (1939) with less than 1% error. To compare these methods in our context, we derive the values of  $k_2$  using our analytical model (Eq. (42)), and by numerical integration of Eqs. (A.6) and (A.11) for our best representative models of Jupiter and Saturn in our grid (although without cores). For Jupiter, our Eq. (42) gives  $k_2 = 0.55$ , the numerical integration gives  $k_2 = 0.57$  to be compared with the measured value of  $k_{2,J} = 0.49$ . For Saturn, these values are 0.60, 0.66 and  $k_{2,S} = 0.32$  respectively. Both models predict  $k_2$  values than are higher than the measured ones. A direct consequence of the presence of heavy elements inside our giant planets. Comparing the models, our Eq. (42) yields slightly smaller  $k_2$  values than the numerical integration which tends to mimic a central over-density (see Sect. 3.2). As discussed above a more precise modeling requires the addition of central enrichment in heavy elements whose mass fraction would be a free parameter. Without better knowledge of the internal composition of giant exoplanets, we think that the two methods yield similar results up to the sought level of accuracy. For sake of completeness, the values of  $k_2$  computed with both methods are presented in Tables B.2 and B.3.

## 4. Polytropic index in gaseous irradiated planets

To readily use the results of Sect. 3, one only needs to have a proper value for the polytropic index  $n$  to be used. In this section, we derive realistic polytropic indices from numerical models of gaseous irradiated planets. All the other polytropic functions

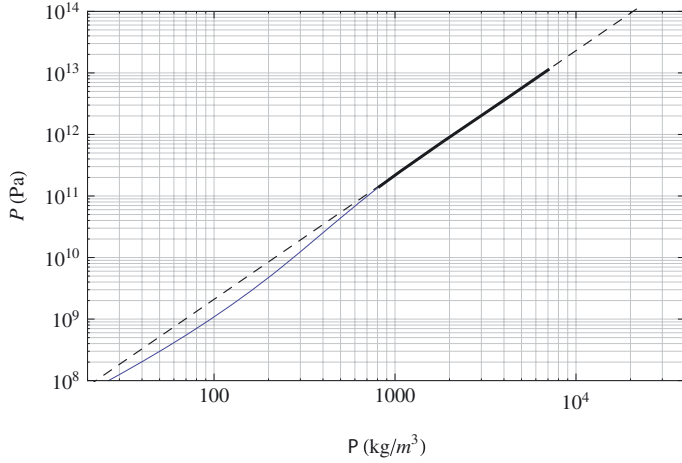


**Fig. 2.** The internal pressure-density profile of an irradiated  $1.8 M_J$  planet (solid line). The dashed line represents the best-fit polytropic equation of state. The pressure-density range covered in the inner part of the body (95% in mass) is represented by the thicker part of the solid curve, which is well modeled by a polytropic EOS. As the thin part of the  $P - \rho$  curve represents only 5% in mass of the body it is disregarded by the fit.

$(\kappa_n, q_n, \dots)$  can be derived by integrating the Lane-Emden equation and are tabulated in Chandrasekhar (1939) and LRS1. They are given for different planetary masses, age and stellar irradiation in Tables B.2 and B.3. We focus on the polytropic index in the planet because, in the context of transiting exoplanets, both the stellar rotation and the stellar tides have a negligible impact on the transit depth, as will be discussed in Sect. 5. The main physics inputs (equations of state, internal composition, irradiated atmosphere models, boundary conditions) used in the present calculations have been described in detail in previous papers devoted to the evolution of extrasolar giant planets (Baraffe et al. 2003; Chabrier et al. 2004; Leconte et al. 2009), and will not be repeated here.

We computed a grid of evolution models of gaseous giant planets with solar composition for various masses  $M_p \in [0.35 M_J, 20 M_J]$  and incoming stellar flux  $F_\star \in [0, 4.18 \times 10^6 \text{ W m}^{-2}]$ . Low irradiation model can be used to infer the oblateness of long period rotating planets (such as Jupiter), while strongly irradiated models can be used to infer the shape and its impact on the transit of close-in planets. For the non irradiated case, the grid extends to  $75 M_J$ . As the effect of irradiation on the internal structure decreases with the effective temperature of the object, these models computed with non irradiated boundary conditions should give a fair description of massive brown dwarfs in the range of irradiation considered. The pressure-density profile of each model is then fitted by a polytropic equation of state (Eq. (3)) at each time step and an example of the result of such a fit is shown in Fig. 2. Note that the disagreement between the actual  $P - \rho$  profile and the polytrope in the lower left area of Fig. 2 is both expected and needed: this low-density region (the first 5% in mass below the atmospheric boundary surface) has a different effective polytropic index than the planetary interior. In order to capture the bulk mechanical property of the planet, we weight each shell in the internal structure profile by its mass during the fitting procedure. This provides us with a grid tabulating the polytropic index of the planet,  $n_p \equiv n_p(M_p, F_\star, t)$ , and its spherical equilibrium radius,  $R_{0,p} \equiv R_{0,p}(M_p, F_\star, t)$ , where  $t$  is the age of the object. These functions, along with other quantities ( $T_{\text{eff}}, \dots$ ), are tabulated in

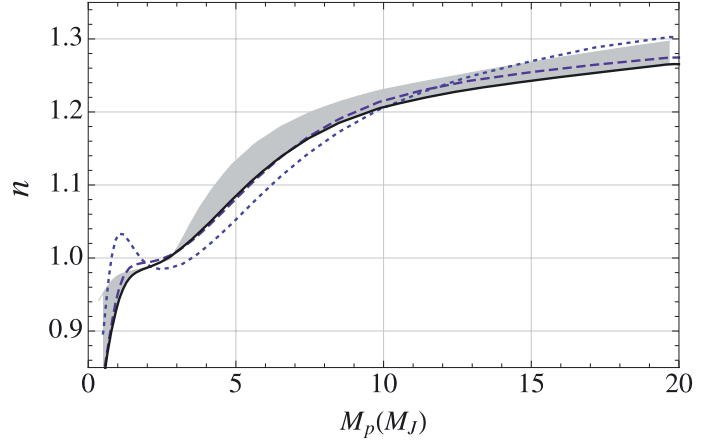


**Fig. 3.** Polytropic index for non-irradiated planets as a function of the planet's mass  $M_p$  at 100 Myr (dotted), 1 Gyr (dashed) and 5 Gyr (solid). The shaded area represents the uncertainty on the polytropic index for the 5 Gyr case (see text).

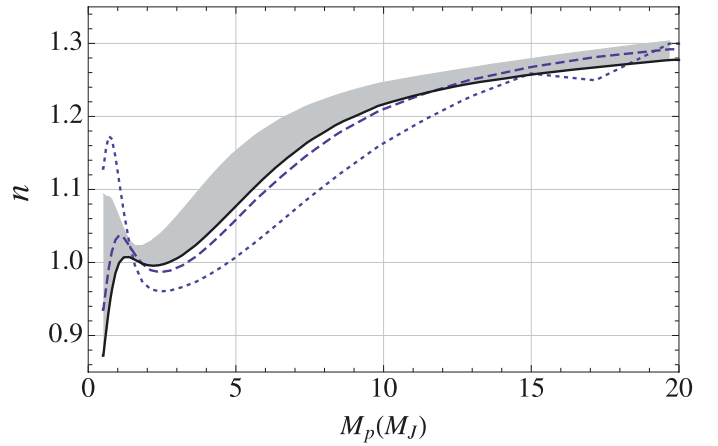


**Fig. 4.** Polytropic index for strongly-irradiated planets as a function of  $M_p$  at 100 Myr (dotted), 1 Gyr (dashed) and 5 Gyr (solid). As the irradiated atmosphere impedes the radiative cooling of the objects, it retards its contraction. Therefore, the non-monotonous behavior observed at the early ages in the non-irradiated case (Fig. 3) is enhanced, even at a later epoch. The bump at the high mass end of the 100 Myr curve is caused by deuterium burning (see text). The shaded area represents the uncertainty on the polytropic index for the 5 Gyr case (see text).

Tables B.2 and B.3<sup>2</sup>. Figures 3 and 4 show the variation of  $n$  with the mass for different ages with  $F_\star = 0$  and  $4.18 \times 10^6 \text{ W m}^{-2}$ , respectively.

As shown in Fig. 3, in the non-irradiated case, we recover qualitatively the results of Chabrier et al. (2009): except for the early stages of the evolution, the (dimensionless) isothermal compressibility of the hydrogen/helium mixture is a monotonically increasing function of the polytropic index,  $\bar{\chi} = \left. \frac{\partial \ln \rho}{\partial \ln P} \right|_T = \frac{n}{1+n}$ , and thus of the mass of the object. In the high mass regime,  $n$  slowly increases as the relative importance of ionic Coulomb effects compared with the degenerate electron pressure decreases, and approaches the  $n = 3/2$  limit, the expected value for a fully degenerate electron gas, when  $M_p$  approaches the hydrogen burning minimum mass ( $\approx 70 M_J$ ) as can be seen in Table B.2. In the low mass regime, the compressibility decreases with

<sup>2</sup> Electronic versions of the model grids are available at [http://perso.ens-lyon.fr/jeremy.leconte/JLSite/JLsite/Exoplanets\\_Simulations.html](http://perso.ens-lyon.fr/jeremy.leconte/JLSite/JLsite/Exoplanets_Simulations.html)

the mass because the repulsive Coulomb potential between the ions, and thus the ionic electrostatic energy becomes dominant. Ultimately, electrostatic effects dominate, leading eventually to  $\bar{\chi} \approx n \approx 0$  for solid, terrestrial planets.

A new feature highlighted by the present calculations is the non-monotonic behavior occurring between 1–3  $M_J$  at early ages. This occurs when the central regions of the planet, of pressure  $P_c$  and temperature  $T_c$ , previously in the atomic/molecular regime, become pressure-ionized, above 1–3 Mbar and 5000–10000 K (Saumon et al. 1995; Chabrier et al. 1992; Saumon et al. 1992), and the electrons become degenerate. An effect more consequential for the lowest mass objects, whose interiors encompass a larger molecular region. This stems from the fact that (Chandrasekhar 1939)

$$P_c > \frac{GM_p^2}{8\pi R_p^4}, \quad \text{and} \quad \frac{GM_J^2}{8\pi R_J^4} \approx 2\text{--}3 \text{ Mbar} \approx P_{\text{ionization}}. \quad (46)$$

Older (with smaller  $R_p$ ) and more massive ( $M_p \gtrsim 2 M_J$ ) objects have  $P_c > 10 P_{\text{ionization}}$  and the ionization extends all the way up to the outermost layers of the gaseous envelope, which then contains a small enough mass fraction of molecular hydrogen to significantly affect the value of the polytropic index. This contrasts with younger objects around 1–3  $M_J$ , whose external molecular hydrogen envelope contains a significant fraction of the planet’s mass, leading to a larger value of the polytropic index, as molecular hydrogen is more compressible than ionized hydrogen (see e.g. Fig. 21 of Saumon et al. 1995). Once again, for these latter objects, the interior structure would be better described by using two different polytropes, but such a significant complication of the calculations is not needed at the presently sought level of accuracy.

As seen in Fig. 4, a strong irradiation enhances the aforementioned feature: the evolution is delayed because the irradiated atmosphere impedes the release of the internal gravothermal energy. This yields a slower contraction, thus a lower central pressure (and lower central temperature) for a longer period so that the object enters the ionization regime at a later epoch. The bump at the high mass end of the 100 Myr isochrone is due to deuterium burning which also occurs later for a given mass, because of the cooler central temperature (see above). At 100 Myr, the 20  $M_J$  has already burned a significant amount of its deuterium content and starts contracting again, whereas lower mass planets are still burning some deuterium supply, leading to a less compact and thus less ionized structure. This leads to the non-monotonic behavior on the high-mass part of the  $n - M$  diagram at 100 Myr, which reflects a similar behavior in the mass-radius relationship.

To evaluate the uncertainty in our determination of the polytropic index, we use an alternative derivation of  $n$ . As shown by Chandrasekhar (1939), the knowledge of  $M$ ,  $K$  and  $n$  is sufficient to infer the radius of the polytrope, with the help of Eq. (24) and the central density, using

$$\rho_c^{\frac{3-n}{2n}} = \frac{M}{4\pi} \left( \frac{4\pi G}{(n+1)K} \right)^{3/2} \left( \xi_1^2 \left| \frac{d\theta}{d\xi} \right|_{\xi_1} \right)^{-1}. \quad (47)$$

Since our numerical simulations provide both the radius,  $R_{0,p}(M_p, F_\star, t)$ , and the central density of the object,  $\rho_{c,p}(M_p, F_\star, t)$ , we can invert Eqs. (24) and (47) to compute  $K_p$  and  $n_p$ . This new determination of the polytropic index is compared with the previous one, obtained by fitting the  $P - \rho$  profile, in Figs. 3 and 4 for the 5 Gyr case: the new  $n_p$  value corresponds to the upper envelope of the shaded area. Figure 3 shows that the

two approaches yield very similar results in the non-irradiated case. For the irradiated case, the average uncertainty on our determination of  $n_p$  lies between about 5% and 15% for the low mass planets.

## 5. Implications for transit measurements

When limb darkening is ignored, the depth of a transit is given by the ratio of the planetary and stellar projected areas. When both bodies are spherical, this simply reduces to  $\delta L_\star / L_\star \propto (R_p / R_\star)^2$ . For close-in planet-star systems, however, both tidal and rotational deformations yield a departure from sphericity, so that what is measured is no longer the mean radius but an *effective* “transit radius” defined such that the cross section of the planet is equal to  $\pi R_{\text{tr},p}^2$  and similarly for the star. Thus the transit depth  $\delta$  reads

$$\delta \equiv \frac{\delta L_\star}{L_\star} = \left( \frac{R_{\text{tr},p}}{R_{\text{tr},\star}} \right)^2. \quad (48)$$

### 5.1. Impact on transit depth

In general, the projected area of an ellipsoid can be computed for any orientation and then at each point of the orbit, as explained in Appendix B. Figure 5 shows the projected area of the planet ( $\pi R_{\text{tr},p}^2$ ) as a function of its anomaly ( $\phi$ ) normalized to the spherical case ( $\pi R_{0,p}^2$ ). When the planet is seen from its “side” ( $\phi / \pi = 0.5$ ), the observer sees a bigger planet because the rotation of the latter on itself tends to increase its volume, as has been mentioned by Li et al. (2010) for WASP-12 b. The possibility to measure these effects from the light curve is discussed in Ragozzine & Wolf (2009) and Carter & Winn (2010a).

For the simple case of an edge-on orbit at mid transit ( $\phi = 0$ ), since the observer, the planet and the star are aligned with the long axis of the tidally deformed ellipsoid<sup>3,4</sup>,  $R_{\text{tr},p} = \sqrt{a_{2,p} a_{3,p}}$  and  $R_{\text{tr},\star} = \sqrt{a_{2,\star} a_{3,\star}}$ . Therefore,

$$\delta = \frac{a_{2,p} a_{3,p}}{a_{2,\star} a_{3,\star}} = \left( \frac{R_{0,p}}{R_{0,\star}} \right)^2 (1 + \eta), \quad (49)$$

where  $R_{0,p}$  and  $R_{0,\star}$  are the respective radii the planet and the star would have in spherical equilibrium and  $\eta$  is by definition the variation of the transit depth induced by the ellipsoidal shape of the components relative to the transit depth in the spherical case. To first order in the deformation, this is given by

$$\eta = \alpha_{2,p} + \alpha_{3,p} - \alpha_{2,\star} - \alpha_{3,\star}. \quad (50)$$

The choice of the expression to be taken for the  $\alpha_i$  depends on the physical context. In the general case, one can use a linear combination of Eqs. (35) and (40) and get a general expression which depends on  $r$ ,  $\omega_p$  and  $\omega_\star$ . However, most of the planet hosting stars have a low rotation rate compared to the orbital mean motion. This entails that the rotational deformation is negligible compared to the tidal one and can generally be neglected. As mentioned in Sect. 3.3, hot Jupiters should be pseudo synchronized early in their evolution. Therefore, we assume such an approximation in our calculations in order not to introduce

<sup>3</sup> This is still verified to first order in  $\phi$  and  $i - \frac{\pi}{2}$  as only second order terms appear.

<sup>4</sup> In the following, the variables have the same meaning as in Sect. 2 and 3 with p indices when referring to the planet and  $\star$  to the star



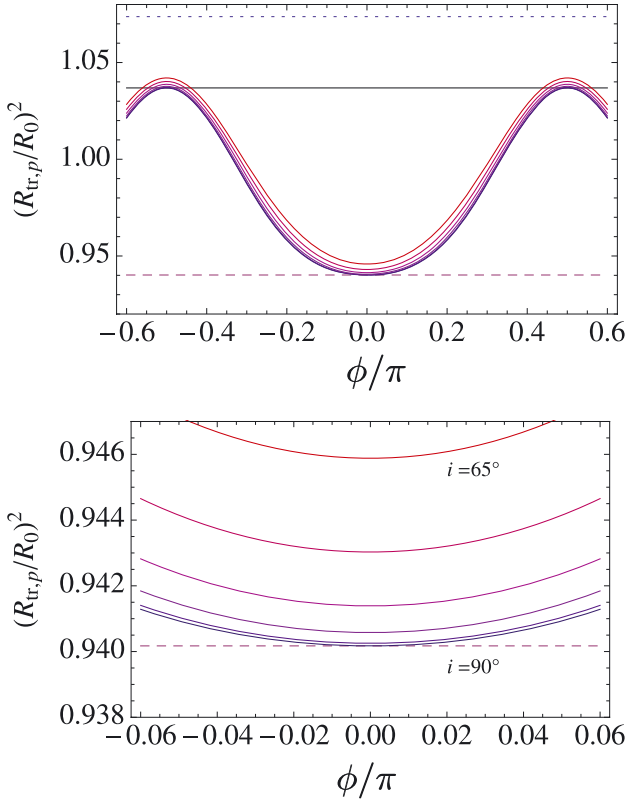


**Fig. 5.** Normalized projected area of the planet as a function of its anomaly ( $\phi$ ) for inclinations of the orbit going from  $i = 90^\circ$  (lowest curve) to  $i = 65^\circ$  (highest curve) by steps of  $5^\circ$  for a WASP-12 b analog on a circular orbit. *Top*: for the full orbit. *Bottom*: zoom on the (primary or secondary) transit. The ordinates of the dotted, solid and dashed horizontal lines are respectively  $a_1 a_2 / R_0^2$  (face-on orbit),  $a_1 a_3 / R_0^2$  and  $a_2 a_3 / R_0^2$ .

any other free parameter. The impact of the rotation alone is described Sect. 3.1. Under such an approximation,

$$\eta = -\frac{1}{3} q_p \left( \frac{1+p}{p} \right) \frac{R_{0,p}^3}{r^3} \left[ \frac{5}{4} \left( \frac{7+p}{1+p} \right) - \left( \frac{4n_p}{3-n_p} \right) \right] + \frac{5}{2} q_\star p \frac{R_{0,\star}^3}{r^3}, \quad (51)$$

where the parameter  $p$  now denotes the mass ratio  $M_p/M_\star$ , and  $q_p$  and  $q_\star$  are equal to  $q_n$  for  $n = n_p$  and  $n = n_\star$ , respectively. The first line in the above equation represents the contribution of the planet, which is always negative (for reasonable values of  $n$ ). Our line of sight follows the long axis of the tidal bulge and we see the minimal cross section of the ellipsoid.

The contribution of the star is positive and, in most cases, negligible compared the planet’s contribution because

$$\frac{R_{0,\star}^3}{R_{0,p}^3} \frac{p^2}{1+p} \ll 1,$$

for a typical system ( $10^{-3}$  for a Jupiter-Sun like system). As a consequence, the results presented hereafter do not depend on  $q_\star$  as long as realistic values of  $n_\star \in [1.5, 3]$  are taken.

Figure 6 portrays the relative transit depth variation computed with Eq. (51) for several planet masses as a function of the orbital distance, for a Sun-like parent star. While all the curves are calculated at an age of 1 Gyr, they do not change much for

older ages because both the radii and the polytropic indices remain nearly unchanged after 1 Gyr (see Fig. 4). Given the accuracy of the radius determination achieved by the latest observations (1 to 10%), the transit depth variation is significant for Saturn mass objects ( $M_p \approx M_J/3$ ) closer than 0.04 AU and Jupiter mass objects closer than 0.02–0.03 AU. Because we derived the equations to first order, the value of  $\eta$  derived from our model should be taken with caution when  $\eta \gtrsim 0.1$ –0.3 (and are clearly not meaningful for  $\eta \gtrsim 1$ ). In this regime, corresponding to the upper left region of Fig. 6, one should use the theory of planetary figures to higher order, but then numerical calculations become necessary, losing the advantage of our simple analytical expressions. Figure 6 also displays the transit depth variation computed for the most distorted known transiting exoplanets, with the observationally measured parameters. The error bars reflect the uncertainties in the model and in the measured data.

## 5.2. Which radius?

Before going further, it is important to summarize the differences between the various radii that we have defined above. In the literature, the term “radius” is used loosely, even for nonspherical objects. Note that this can lead to discrepant normalizations throughout different studies and published values of transit radius measurements when, for example, radii are shown in units of Jupiter radii ( $R_J$ ) without precisely defining the latter.

One can define  $a_1$ ,  $a_2$  and  $a_3$  as the distances between the center and some isobar surface along the three principal axes of inertia. For any distorted object, we can define the mean radius ( $R$ ) as the radius of the sphere that would enclose the same volume as the described surface. In our case of a general ellipsoid, we have  $R = (a_1 a_2 a_3)^{1/3}$ . If axial symmetry holds (e.g. for a rotating fluid body), we have  $a_1 = a_2 \equiv R_{\text{eq}}$ , defining the equatorial radius, and  $a_3 \equiv R_{\text{pol}}$  the polar radius. Finally,  $R_0$  is the radius of the spherical shape that the fluid body would assume if it was isolated and at rest in an inertial frame (the limiting case for which all the mentioned radii would be equal). This latter is the radius computed in usual 1D numerical evolution calculations. Note that in general  $R \neq R_0$  because the centrifugal force has a net outward component that increases the volume of the object, as can be seen from Eq. (33).

One must be aware that only  $a_1$ ,  $a_2$  and  $a_3$  (reducing to  $R_{\text{eq}}$  and  $R_{\text{pol}}$  for solar system gaseous bodies) can be measured directly and are *not* model dependent. This is why we define  $R_J$  as the equatorial radius of Jupiter at the 1 bar level ( $R_J \equiv R_{\text{eq},J} = 7.1492 \times 10^7 \text{m}$ , Guillot 2005, and reference therein).

Unfortunately, transit measurements only give access to the projected opaque cross section of the planet ( $\equiv \pi R_{\text{tr},p}^2$ ) defining a “transit radius” which depends on the shape of the planet, its orientation during the observation and the wavelength used. To convert this transit radius inferred from the observations ( $R_{\text{tr},p}$ ) to the spherical radius ( $R_{0,p}$ ) – that can be compared to 1D numerical models – one must eliminate  $\delta$  from Eqs. (48) and (49). As shown above, the stellar impact on  $\eta$  is negligible compared to the planet’s contribution ( $R_{\text{tr},\star} \approx R_{0,\star}$ ). Then, using the first term in Eq. (51) and expanding the expression giving the definition of  $R_{\text{tr},p}$ , one gets

$$\begin{aligned} R_{0,p} &\approx R_{\text{tr},p} \left( 1 - \frac{1}{2} (\alpha_{2,p} + \alpha_{3,p}) \right) \\ &\approx R_{\text{tr},p} \left( 1 - \frac{\eta}{2} \right). \end{aligned} \quad (52)$$

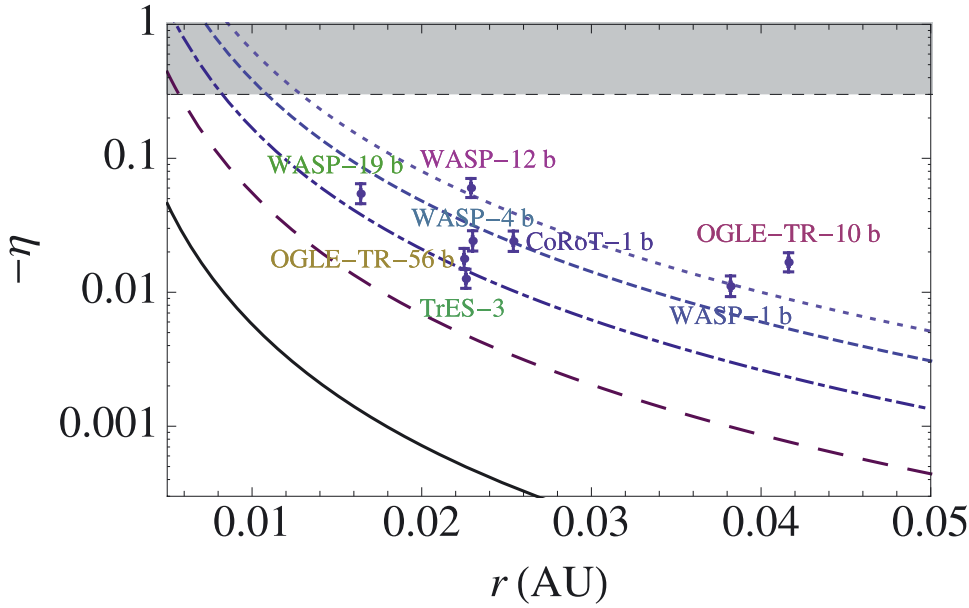


**Fig. 6.** Relative transit depth variation  $\eta$  computed with Eq. (51) as a function of the semimajor axis at 1 Gyr for planets of mass:  $0.3 M_J$  (dotted),  $0.5 M_J$  (dashed),  $1 M_J$  (dash-dotted),  $3 M_J$  (long dashed),  $15 M_J$  (solid). The shaded area shows the zone where higher order terms become non-negligible. The decrease in the transit depth due to tidal interactions is smaller when the mass of the planet increases because massive objects are more compressible (see Sect. 4) and thus less subject to nonspherical deformations.

For the most distorted known planets, the relative variation between the transit radius and the equilibrium radius

$$\Delta R \equiv (R_{0,p} - R_{tr,p})/R_{tr,p} \approx -\eta/2$$

is positive and amounts to 3.00% for WASP-12 b, 2.72% for WASP-19 b, 1.21% for WASP-4 b, 1.20% for CoRoT-1 b, 0.89% and OGLE-TR-56 b.

Of course, since

$$\eta \propto \left(\frac{1+p}{p}\right) \frac{R_{0,p}^3}{r^3}, \quad (53)$$

Eq. (52) is an implicit equation on  $R_{0,p}$ . To obtain  $R_{0,p}$  to the sought accuracy, a perturbative development in powers of  $\eta_{tr} = \eta(R_{0,p} = R_{tr,p})$  can be obtained using recursively Eq. (52)

$$\begin{aligned} \frac{R_{0,p}}{R_{tr,p}} &\approx 1 - \frac{\eta(R_{0,p})}{2} \\ &\approx 1 - \frac{\eta_{tr}}{2} + \frac{3\eta_{tr}^2}{4} - \frac{3\eta_{tr}^3}{2} + \mathcal{O}(\eta_{tr}^4). \end{aligned} \quad (54)$$

However, terms of order  $\eta_{tr}^2$  are of the same order than the second order corrections to the shape that we have neglected throughout.

## 6. Conclusion

Because of the large variety of exoplanetary systems presently discovered, with many more expected in the near future, and the increasing accuracy of the observations, it is important to take into account the corrections arising from the nonspherical deformation of the planet or the star, due to rotational and/or tidal forces, as such a deformation yields a decrease in the transit depth. In order to do so, it is extremely useful to be able to compute *analytically* the shape of planets and stars in any configuration from the knowledge of only their mass, orbital separation and one single parameter describing their internal structure, namely the polytropic index,  $n$ . Such formulae are derived in Sect. 3, and can be easily used to determine the impact of the shape of the planet on its phase curve and on the shape of the transit light curve itself (Carter & Winn 2010a). They can also

be used to model ellipsoidal variations of the stellar flux that are now detected in the CoRoT and Kepler light curves (Welsh et al. 2010). These formulae also give good approximations for various parameters describing the mass redistribution in the body's interior and the response to a perturbing gravitational field, i.e. the moment of inertia,  $I$ , and the Love number of second degree  $k_2$ .

Another major implication of the present work is to show that departure from sphericity of the transiting planets produces a bias in the determination of the radius. For the closest planets detected so far ( $\leq 0.05$  AU), the effect on the transit depth is of the order of 1 to 10% (see Fig. 4), by no means a negligible effect. The equilibrium radius of these strongly distorted objects can thus be larger than the measured radius, inferred from the area of the (smaller) cross section presented to the observer by the planet during the transit. The analytical formulae derived in the present paper, and the characteristic polytropic index values derived for various gaseous planet masses and ages, make possible to easily take such a correction into account. Interestingly, since this equilibrium radius is the one computed with the 1D structure models available in the literature, the bias reported here still enhances the magnitude of the puzzling radius anomaly (see Fig. 6 of Lecante et al. 2010) exhibited by the so-called bloated planets.

*Acknowledgements.* The authors acknowledge the hospitality of the Kavli Institute for Theoretical Physics at UCSB (funded by the NSF through Grant PHY05-51164), where this work started. This work has been supported in part by NASA Grant NNX07AG81G and NSF grants AST 0707628. We also acknowledge funding from the European Community via the P7/2007-2013 Grant Agreement No. 247060. The authors are grateful to the anonymous referee for his/her sharp and enlightening comments.

## Appendix A: Theory of planetary figures: numerical methods

Here, we briefly outline the method described in Sterne (1939) to compute numerically the response of a body in hydrostatic equilibrium to a perturbing potential<sup>5</sup> and derive additional formulae.

<sup>5</sup> Here we take the convention that the force acting on a particule of mass  $M$  due to a potential  $V$  is  $\mathbf{F} = -M\mathbf{grad}V$ . This yields some difference of signs with Sterne (1939).

To lowest order (which is consistent with the order of approximation used throughout the present paper) the body response is linear and the total deformation is the sum of the response to each term of the decomposition of the perturbing potential. Let us consider a term of the decomposition of the potential of the form

$$V_1^m(r, \theta, \psi) = c_1^m r^l Y_1^m(\theta, \psi), \quad (\text{A.1})$$

where the  $Y_1^m$  are tesseral harmonics defined by

$$Y_1^m(\theta, \psi) = \begin{cases} \cos |m|\psi \\ \sin |m|\psi \end{cases} P_1^{|m|}(\cos \theta). \quad (\text{A.2})$$

The  $\cos$  ( $\sin$ ) corresponds to positive (negative) values of  $m$  and  $P_1^m$  are the usual associated Legendre polynomials. The reference axis defining  $\theta$  and  $\psi$  may change from one term to the other. For example, the rotation axis is best suited to treat rotational distortion and the line connecting the center of mass of each body is better to describe the tidal distortion. It is shown by [Sterne \(1939\)](#) that to first order, the shape of the distorted level surface of mean radius  $s$  (see [Zharkov & Trubitsyn 1980](#), for a detailed definition) takes the form

$$r(s, \theta, \psi) = s \left( 1 + s_1^m(s) Y_1^m(\theta, \psi) \right), \quad (\text{A.3})$$

where  $r$  is the distance between the center and the level surface as a function of  $\theta$  and  $\psi$  and  $s_1^m(s)$  a figure function yet to be calculated. [Sterne \(1939\)](#) shown that, ignoring terms of order  $s_1^m \times s_1^m$ ,  $s_1^m$  verifies the following differential equation

$$\frac{d^2 s_1^m}{ds^2} - \frac{1(1+1)}{s^2} s_1^m + \frac{6}{s^2} \frac{\rho(s)}{\bar{\rho}(s)} \left( s \frac{ds_1^m}{ds} + s_1^m \right) = 0, \quad (\text{A.4})$$

with

$$\bar{\rho}(s) = \frac{3}{s^3} \int_0^s \rho(s') s'^2 ds'. \quad (\text{A.5})$$

Using the variable  $\eta_1(s) = \frac{s}{s_1^m(s)} \frac{ds_1^m}{ds}$ , this rewrites

$$s \frac{d\eta_1}{ds} + \eta_1^2 - \eta_1 - 1(1+1) + 6 \frac{\rho(s)}{\bar{\rho}(s)} (\eta_1 + 1) = 0. \quad (\text{A.6})$$

Then,  $\eta_1(R)$  ( $R$  being the external mean radius of the object) can be obtained by numerical integration (with  $\eta_1(0) = 1-2$ ) and the shape and external potential ( $U_1^m$ ) of the body are given by, respectively

$$s_1^m(R) = -\frac{2l+1}{1+\eta_1(R)} \frac{1}{MG} c_1^m R^{l+1} \quad (\text{A.7})$$

and

$$U_1^m(r, \theta, \psi) = \frac{1+1-\eta_1(R)}{1+\eta_1(R)} \frac{R^{2l+1}}{r^{l+1}} c_1^m Y_1^m(\theta, \psi). \quad (\text{A.8})$$

In order to compare this numerical model with others, we can compute several observable quantities. By definition, the potential Love number of degree 2 ( $k_2$ ) is given by

$$U_2^0(R, \theta, \psi) = k_2 V_2^0(R, \theta, \psi), \quad (\text{A.9})$$

which yields

$$k_2 = \frac{3 - \eta_2(R)}{2 + \eta_2(R)}. \quad (\text{A.10})$$

The level Love number ( $h_2$ ) is given by

$$s_2^0(R) Y_2^0(\theta, \psi) = -h_2 \frac{V_2^0(R, \theta, \psi)}{gR}, \quad (\text{A.11})$$

where  $g$  is the surface gravity acceleration, and

$$h_2 = \frac{5}{2 + \eta_2(R)} = k_2 + 1, \quad (\text{A.12})$$

as expected for a body in hydrostatic equilibrium.

### A.1. Axi-symmetric case

Thus the first gravitational moment ( $J_2$ ) defined by

$$U_2^0(r, \theta, \psi) = J_2 \frac{GM}{r} \left( \frac{R_{\text{eq}}}{r} \right)^2 P_2^0(\cos \theta), \quad (\text{A.13})$$

is given by

$$J_2 = k_2 \frac{R^3}{GM} c_1^m. \quad (\text{A.14})$$

No distinction is made between  $R$  and  $R_{\text{eq}}$  (the equatorial radius) when comparing Eqs. (A.8) and (A.13) because this would only add higher order corrections to  $J_2$  which is already a first order quantity.

For the rotational distortion of the body whose angular velocity is  $\omega$ ,  $c_2^0 = \omega^2/3$  and

$$J_2 = \frac{k_2 \omega^2 R^3}{3 GM}. \quad (\text{A.15})$$

If one is concerned with the external shape, the oblateness ( $f$ , see Eq. (36)) of a rotating body is given by

$$\begin{aligned} f &= -\frac{3}{2} s_2^0 \\ &= \frac{h_2 \omega^2 R^3}{2 GM} = \frac{k_2 + 1}{2} \frac{\omega^2 R^3}{GM}. \end{aligned} \quad (\text{A.16})$$

By extension, one can define  $J_2$  for a tidal perturbation by a secondary of mass  $M'$  at a distance  $r'$ ,  $c_2^0 = -\frac{GM'}{r'^3}$  leading to

$$J_2 = -k_2 \frac{M'}{M} \left( \frac{R}{r'} \right)^3, \quad (\text{A.17})$$

but the reference axis is the line connecting the two center of mass and not the rotational axis.

### A.2. Triaxial case

While it is tempting to add Eqs. (A.15) and (A.17) to obtain the total  $J_2$  of a body in a close binary, we must remember that the tidal and rotational deformations do not have the same axis of symmetry in general. Taking  $\theta$  as the colatitude and  $\psi$  as the longitude of the body considered, the external gravitational field of the latter reads

$$\begin{aligned} U(r, \theta, \psi) &= -\frac{GM}{r} \\ &\times \sum_{l=0}^{\infty} \sum_{m=0}^l \left( \frac{R_{\text{eq}}}{r} \right)^l (C_1^m \cos m\psi + S_1^m \sin m\psi) P_l^m(\cos \theta). \end{aligned} \quad (\text{A.18})$$

The quadrupole moment in the linear approximation, is given at the surface by

$$-\frac{GM}{R_{\text{eq}}} \sum_{m=0}^2 (C_2^m \cos m\psi + S_2^m \sin m\psi) P_2^m(\cos \theta) = k_2 R_{\text{eq}}^2 \left( \frac{\omega^2}{3} P_2^0(\cos \theta) - \frac{GM'}{r'^3} P_2^0(\cos \theta') \right), \quad (\text{A.19})$$

where  $\theta'$  is the angle between the current point and the line connecting the two center of mass. For the coplanar case where the tides raising object orbits in the equatorial plane of the distorted body,  $\cos \theta' = \sin \theta \cos \psi$  and thus

$$P_2^0(\cos \theta') = \frac{3}{4} \sin^2(\theta) \cos(2\psi) + \frac{3 \sin^2(\theta)}{4} - \frac{1}{2} = \frac{1}{4} \cos(2\psi) P_2^2(\cos \theta) - \frac{1}{2} P_2^0(\cos \theta). \quad (\text{A.20})$$

Thus

$$J_2 = -C_2^0 = k_2 \left[ \frac{1}{3} \frac{\omega^2 R_{\text{eq}}^3}{GM} + \frac{1}{2} \frac{M'}{M} \left( \frac{R}{r'} \right)^3 \right], \quad (\text{A.21})$$

and

$$C_2^2 = -k_2 \frac{1}{4} \frac{M'}{M} \left( \frac{R}{r'} \right)^3. \quad (\text{A.22})$$

All the other moments are equal to 0. Similar decompositions can be used to infer the precise shape of the surface from a sum of perturbing fields. This gives

$$\frac{r(R, \theta, \psi)}{R} = 1 - h_2 \left( \frac{1}{2} \frac{M'}{M} \left( \frac{R}{r'} \right)^3 + \frac{1}{3} \frac{\omega^2 R^3}{GM} \right) P_2^0(\cos \theta) + h_2 \left( \frac{1}{4} \frac{M'}{M} \left( \frac{R}{r'} \right)^3 \right) \cos(2\psi) P_2^2(\cos \theta), \quad (\text{A.23})$$

which directly translates into  $a_1$ ,  $a_2$  and  $a_3$  (once  $R$  is known) by setting  $(\theta, \psi)$  equal to  $(\pi/2, 0)$ ,  $(\pi/2, \pi/2)$  and  $(0, 0)$ , respectively. Translating this into  $a_1$ ,  $a_2$  and  $a_3$  is a little more complicated because one needs to account for the fact that  $R > R_0$  due to the centrifugal potential. This can be taken into account either numerically – by including the centrifugal force when solving the hydrostatic equilibrium – or analytically using Eq. (32) or (45).

## Appendix B: Projected area of a triaxial ellipsoid

### B.1. General case

Let us define two coordinate systems. The first one  $(\hat{x}', \hat{y}', \hat{z}')$  is defined by the three main axes of the ellipsoid. In this frame, the equation of the surface of the ellipsoid is

$$\frac{x'^2}{a_1^2} + \frac{y'^2}{a_2^2} + \frac{z'^2}{a_3^2} = 1. \quad (\text{B.1})$$

To compute the projected area of this ellipsoid as it will be seen by the observer, it is easier to put ourselves in another coordinate system defined by the line connecting the center of mass of the system and the observer (toward the observer;  $\hat{x}$ ), the projection of the orbital angular momentum on the sky plane ( $\hat{z}$ ) and a third axis in the sky plane chosen so that  $(\hat{x}, \hat{y}, \hat{z})$  follows the right-hand vector sense. The current position vector ( $\mathbf{r} = (x, y, z)$ )

expressed in this frame is thus related to the one expressed in the first coordinate system by a rotation matrix  $\mathcal{R}$  such as

$$\mathbf{r}' = \mathcal{R} \cdot \mathbf{r}, \quad (\text{B.2})$$

With  $\mathcal{R}^{\text{tr}} \mathcal{R} = \mathbf{1}$ . The equation of the ellipsoid in the new system thus writes

$$g(\mathbf{r}) \equiv \mathbf{r}'^{\text{tr}} \mathcal{R}^{\text{tr}} \begin{pmatrix} \frac{1}{a_1^2} & 0 & 0 \\ 0 & \frac{1}{a_2^2} & 0 \\ 0 & 0 & \frac{1}{a_3^2} \end{pmatrix} \mathcal{R} \mathbf{r} \equiv \mathbf{r}'^{\text{tr}} \mathcal{A} \mathbf{r} = 1. \quad (\text{B.3})$$

The exact value of the matrix  $\mathcal{A}$  will depend on the rotation needed and on the angles chosen to represent it. This can be worked out in each specific case. To keep some generality, we take  $\mathcal{A}$  of the form

$$\mathcal{A} = \begin{pmatrix} a & d & f \\ d & b & e \\ f & e & c \end{pmatrix}. \quad (\text{B.4})$$

The symmetry is ensured by the fact that both of our coordinate systems are orthonormal. The equation of the contour of the projected shadow is given by the fact that the normal to the ellipsoid is normal to the line of sight ( $\hat{x}$ ) there. This assumes a completely opaque body below the isobar chosen to be the surface. The complete calculation of the level at which optical rays that are grazing, at the terminator, have an optical depth close to unity (Hubbard et al. 2001; Burrows et al. 2003; Guillot 2010) – in the present geometry – should give rise to subtle effects but of smaller importance. This reads

$$0 = \mathbf{grad}[g(\mathbf{r})]^{\text{tr}} \cdot \hat{x} = 2 \mathbf{r}'^{\text{tr}} \mathcal{A} \hat{x}. \quad (\text{B.5})$$

This shows that these points are located on a plane whose equation is (since  $a \neq 0$ )

$$x = \frac{1}{a} (d y + f z). \quad (\text{B.6})$$

Substituting  $x$  in Eq. (B.3) by Eq. (B.6) we see that the cross section is an ellipse following the equation

$$(y, z) \begin{pmatrix} b + 3\frac{d^2}{a} & e + 3\frac{df}{a} \\ e + 3\frac{df}{a} & c + 3\frac{f^2}{a} \end{pmatrix} \begin{pmatrix} y \\ z \end{pmatrix} \equiv (y, z) \mathcal{B} \begin{pmatrix} y \\ z \end{pmatrix} = 1. \quad (\text{B.7})$$

It is thus possible to find the rotation in the sky plane needed to reduce the ellipse and find its principal axes ( $p_1$ ,  $p_2$ ). If only the cross section ( $\pi p_1 p_2$ ) is needed, we can use the fact that the determinant of a matrix is independent of the coordinate system so that

$$\pi p_1 p_2 = \frac{\pi}{\sqrt{\text{Det}(\mathcal{B})}}, \quad (\text{B.8})$$

with

$$\text{Det}(\mathcal{B}) = \frac{3bf^2}{a} + \frac{3cd^2}{a} - \frac{6def}{a} + bc - e^2. \quad (\text{B.9})$$

In the case of an edge-on orbit at mid transit, no rotation is needed,  $\mathcal{R}$  is the identity and thus  $a = 1/a_1^2$ ,  $b = 1/a_2^2$ ,  $c = 1/a_3^2$  and  $d = e = f = 0$ . We retrieve

$$\pi p_1 p_2 = \frac{\pi}{\sqrt{bc}} = \pi a_2 a_3. \quad (\text{B.10})$$

**Table B.1.** Summary of variables.

Symbol	Definition	Equation
$E$	total energy	(1)
$U$	internal energy	(5)
$W$	self gravitational energy	(6)
$T$	total kinetic energy	(11)
$T_s$	rotational kinetic energy	(12)
$T_0$	orbital kinetic energy	(16)
$W_i$	gravitational interaction energy	(17)
$n, K$	polytropic index and temperature	(3)
$G$	gravitational constant	
$M$	mass of primary	
$R$	mean radius of the primary	
$P$	pressure	
$\rho$	density	
$a_i$	principal axes of the ellipsoid	
$\alpha_i$	first order correction to $a_i$	(27)
$r$	orbital distance	
$\lambda_i$	asymmetry factor = $(a_3/a_i)^{2/3}$	
$\rho_c$	central density	(5)
$\bar{k}_1$	scaling constant of the internal energy	(5), (7)
$\bar{k}_2$	scaling constant of the gravitational energy	(6), (8)
$\bar{f}$	ellipsoidal correction to the gravitational energy	(6), (9)
$A_i$		(10)
$I$	principal moment of inertia	(14), (30)
$\kappa_n$	dimensionless moment of inertia	(13)
$\Omega$	orbital mean motion	(16), (19)
$\Lambda$	internal angular velocity of the fluid	(12)
$\omega$	rotational angular velocity	(15)
$\xi_1$	dimensionless radius (see Chandrasekhar 1939)	(7)
$\theta'_1$	dimensionless density derivative (see Chandrasekhar 1939)	(7)
$I_{ij}$	Inertia tensor	(18)
$\delta_{ij}$	Kronecker symbol	
$\Delta$		(19)
$g_i$		(22)
$R_0$	radius of the <i>unperturbed</i> spherical polytrope	(24)
$q_n$	= $\kappa_n(1 - \frac{n}{5})$	(25), (26)
$\mu_R$	= $GM'/r^3$	(25), (26)
$\bar{\mu}_R$	$\mu_R/(\pi G \bar{\rho})$	(25), (26)
$\bar{\rho}$	mean density	
$\bar{\omega}$	dimensionless angular velocity	(31)
$f$	oblateness	(36)
$J_2$	quadrupolar gravitational moment	(37)
$k_2$	Love number (half the apsidal motion constant)	(42)
$L_\star$	stellar luminosity out of transit	(48)
$\delta L_\star$	stellar luminosity variation in transit	(48)
$\delta$	relative transit depth	(48)
$R_{tr}$	transit radius	(48)
$\eta$	non spherical contribution to the transit depth	(49)

## B.2. Coplanar case

If the planet equator and the orbital plane are coplanar, the unit vectors of first coordinate system defined above coincides with the unit vectors defined by the line connecting the two center of mass (from the secondary to the object under consideration;  $\hat{x}'$ ), its normal in the orbital plane (in the direction of motion;  $\hat{y}'$ ) and the rotation axis of the body ( $\hat{z}'$ ). If  $i$  is the inclination of the orbit with respect to the sky plane and  $\phi$  the true anomaly defined to be 0 at mid transit, the rotation matrix defined by Eq. (B.2) reads

$$\mathcal{R} = \begin{pmatrix} \sin(i) \cos(\phi) & \sin(\phi) & \cos(i) \cos(\phi) \\ -\sin(i) \sin(\phi) & \cos(\phi) & -\cos(i) \sin(\phi) \\ -\cos(i) & 0 & \sin(i) \end{pmatrix}. \quad (\text{B.11})$$

The  $\mathcal{A}$  matrix can be computed thanks to Eq. (B.3) giving the  $a, b, \dots, f$  coefficients and thus  $\text{Det}(\mathcal{B})$ . This gives the project area

of the planet or the star at any given point of the orbit as shown on Fig. 5.

## References

- Baraffe, I., Chabrier, G., Barman, T. S., Allard, F., & Hauschildt, P. H. 2003, *A&A*, 402, 701
- Burrows, A., Sudarsky, D., & Hubbard, W. B. 2003, *ApJ*, 594, 545
- Carter, J. A., & Winn, J. N. 2010a, *ApJ*, 709, 1219
- Carter, J. A., & Winn, J. N. 2010b, *ApJ*, 716, 850
- Chabrier, G., Baraffe, I., Leconte, J., Gallardo, J., & Barman, T. 2009, in *AIP Conf. Ser.* 1094, ed. E. Stempels, 102
- Chabrier, G., Barman, T., Baraffe, I., Allard, F., & Hauschildt, P. H. 2004, *ApJ*, 603, L53
- Chabrier, G., Saumon, D., Hubbard, W. B., & Lunine, J. I. 1992, *ApJ*, 391, 817
- Chandrasekhar, S. 1939, *An introduction to the study of stellar structure* (Chicago, Ill.: The University of Chicago press)
- Darwin, G. H. 1908, *Scientific Papers* (New York: Cambridge University Press)

- Deming, D., Harrington, J., Laughlin, G., et al. 2007, *ApJ*, 667, L199  
Goldreich, P., & Soter, S. 1966, *Icarus*, 5, 375  
Guillot, T. 2005, *Ann. Rev. Earth Planet. Sci.*, 33, 493  
Guillot, T. 2010, *A&A*, 520, A27  
Hubbard, W. B., Fortney, J. J., Lunine, J. I., et al. 2001, *ApJ*, 560, 413  
Hut, P. 1981, *A&A*, 99, 126  
Lai, D., Rasio, F. A., & Shapiro, S. L. 1993, *ApJS*, 88, 205  
Lai, D., Rasio, F. A., & Shapiro, S. L. 1994, *ApJ*, 423, 344  
Lecante, J., Baraffe, I., Chabrier, G., Barman, T., & Levrard, B. 2009, *A&A*, 506, 385  
Lecante, J., Chabrier, G., Baraffe, I., & Levrard, B. 2010, *A&A*, 516, A64  
Li, S., Miller, N., Lin, D. N. C., & Fortney, J. J. 2010, *Nature*, 463, 1054  
Love, A. E. H. 1909, *MNRAS*, 69, 476  
Ragozzine, D., & Wolf, A. S. 2009, *ApJ*, 698, 1778  
Saumon, D., Hubbard, W. B., Chabrier, G., & van Horn, H. M. 1992, *ApJ*, 391, 827  
Saumon, D., Chabrier, G., & van Horn, H. M. 1995, *ApJS*, 99, 713  
Sterne, T. E. 1939, *MNRAS*, 99, 451  
Welsh, W. F., Orosz, J. A., Seager, S., et al. 2010, *ApJ*, 713, L145  
Zharkov, V. N., & Trubitsyn, V. P. 1980, *The Physics of Planetary Interiors*, ed. V. N. Zharkov, & V. P. Trubitsyn  
Zharkov, V. N., Makalkin, A. B., & Trubitsyn, V. P. 1973, *Sov. Astron.*, 17, 97

**Table B.2.** Model parameters for non-irradiated planets of various masses.

$M_p (M_J)$	Age (Gyr)	$R_{0,p} (R_J)$	$T_{\text{eff}} (K)$	$P_c (\text{MBar})$	$T_c (K)$	$\rho_c (\text{kg/m}^3)$	$n$	$\kappa_n$	Analytic	$k_2$ Numeric
0.35	0.05	1.1579	235.6	2.87	15 324.	1016.	0.913	0.681	0.568	0.428
0.35	0.10	1.0923	194.6	3.26	13 566.	1109.	0.868	0.694	0.598	0.478
0.35	0.50	0.9934	118.4	4.05	9698.	1292.	0.801	0.715	0.645	0.578
0.35	1.00	0.9801	93.4	4.18	9142.	1326.	0.792	0.718	0.651	0.594
0.35	5.00	0.9501	58.9	4.50	7758.	1402.	0.771	0.725	0.667	0.631
0.5	0.05	1.1730	280.9	5.40	19 045.	1394.	0.946	0.670	0.547	0.445
0.5	0.10	1.1112	234.8	6.06	16 765.	1507.	0.897	0.686	0.579	0.495
0.5	0.50	1.0165	140.2	7.47	12 120.	1742.	0.838	0.704	0.618	0.578
0.5	1.00	0.9961	108.4	7.91	10 950.	1811.	0.834	0.705	0.621	0.595
0.5	5.00	0.9682	62.4	8.53	9160.	1918.	0.824	0.708	0.628	0.624
0.6	0.05	1.1809	302.0	7.67	21 971.	1670.	0.987	0.658	0.522	0.443
0.6	0.10	1.1233	254.0	8.51	19 377.	1795.	0.936	0.674	0.553	0.490
0.6	0.50	1.0292	153.9	10.44	13 816.	2067.	0.869	0.694	0.597	0.571
0.6	1.00	1.0063	120.0	11.06	12 332.	2146.	0.861	0.697	0.602	0.591
0.6	5.00	0.9775	66.7	12.01	10 196.	2278.	0.856	0.698	0.606	0.616
0.7	0.05	1.1842	322.0	10.44	25 065.	1945.	1.021	0.648	0.501	0.440
0.7	0.10	1.1313	271.9	11.50	22 040.	2090.	0.974	0.662	0.529	0.484
0.7	0.50	1.0390	166.9	14.00	15 781.	2398.	0.901	0.684	0.576	0.562
0.7	1.00	1.0155	129.9	14.79	13 766.	2492.	0.887	0.688	0.585	0.583
0.7	5.00	0.9849	71.0	16.13	11 251.	2644.	0.882	0.690	0.589	0.607
0.8	0.05	1.1857	339.9	13.64	28 043.	2218.	1.044	0.641	0.488	0.439
0.8	0.10	1.1360	285.7	14.98	24 692.	2374.	1.003	0.654	0.512	0.478
0.8	0.50	1.0466	178.8	18.13	17 626.	2728.	0.929	0.676	0.558	0.553
0.8	1.00	1.0224	139.5	19.22	15 272.	2846.	0.912	0.681	0.568	0.574
0.8	5.00	0.9903	76.1	20.96	12 243.	3022.	0.903	0.684	0.575	0.599
0.9	0.05	1.1864	355.5	17.22	30 999.	2469.	1.057	0.637	0.480	0.438
0.9	0.10	1.1393	297.1	18.84	27 295.	2641.	1.021	0.648	0.501	0.475
0.9	0.50	1.0525	189.6	22.83	19 399.	3048.	0.952	0.669	0.543	0.546
0.9	1.00	1.0272	148.9	24.30	16 774.	3191.	0.933	0.674	0.555	0.567
0.9	5.00	0.9946	82.0	26.53	13 201.	3402.	0.921	0.678	0.563	0.592
1.0	0.05	1.1873	369.1	21.02	33 873.	2696.	1.061	0.636	0.478	0.440
1.0	0.10	1.1419	306.5	23.04	29 826.	2897.	1.030	0.645	0.496	0.474
1.0	0.50	1.0576	199.5	27.98	21 165.	3357.	0.970	0.663	0.532	0.540
1.0	1.00	1.0316	157.6	29.88	18 218.	3528.	0.951	0.669	0.544	0.560
1.0	5.00	0.9980	87.0	32.77	14 132.	3779.	0.936	0.673	0.553	0.585
1.2	0.05	1.1902	397.7	29.16	39 189.	3127.	1.051	0.639	0.484	0.445
1.2	0.10	1.1467	328.1	32.22	34 685.	3384.	1.032	0.645	0.495	0.475
1.2	0.50	1.0666	216.9	39.33	24 692.	3949.	0.992	0.657	0.519	0.530
1.2	1.00	1.0396	173.3	42.28	21 047.	4173.	0.975	0.662	0.529	0.550
1.2	5.00	1.0037	96.0	46.87	15 917.	4513.	0.960	0.666	0.538	0.574
1.5	0.05	1.1974	437.2	43.27	46 493.	3761.	1.019	0.648	0.502	0.456
1.5	0.10	1.1541	362.0	48.34	41 254.	4096.	1.016	0.650	0.504	0.479
1.5	0.50	1.0768	238.7	59.61	29 797.	4811.	0.998	0.655	0.515	0.524
1.5	1.00	1.0496	193.9	64.49	25 342.	5108.	0.989	0.658	0.520	0.541
1.5	5.00	1.0103	108.2	72.65	18 523.	5584.	0.976	0.661	0.528	0.563
1.8	0.05	1.2044	467.7	59.79	53 447.	4405.	0.994	0.656	0.517	0.465
1.8	0.10	1.1613	392.9	67.23	47 612.	4816.	0.999	0.655	0.514	0.484
1.8	0.50	1.0853	257.2	83.49	34 881.	5679.	0.997	0.655	0.515	0.521
1.8	1.00	1.0575	211.6	90.76	29 639.	6049.	0.993	0.656	0.518	0.535
1.8	5.00	1.0157	119.2	103.42	21 166.	6665.	0.984	0.659	0.524	0.556
2.1	0.05	1.2098	493.7	79.29	60 248.	5071.	0.980	0.660	0.526	0.471
2.1	0.10	1.1680	420.3	89.18	54 147.	5542.	0.989	0.658	0.521	0.487
2.1	0.50	1.0920	272.9	111.54	39 939.	6568.	0.996	0.656	0.516	0.518
2.1	1.00	1.0639	227.4	121.62	33 971.	7009.	0.995	0.656	0.517	0.530
2.1	5.00	1.0199	129.6	139.84	23 851.	7773.	0.988	0.658	0.521	0.550
3.0	0.05	1.2203	578.7	156.52	83 329.	7108.	0.980	0.660	0.526	0.480
3.0	0.10	1.1803	488.6	176.70	74 971.	7806.	0.989	0.658	0.520	0.490
3.0	0.50	1.1031	316.3	225.68	55 401.	9414.	1.006	0.652	0.510	0.510
3.0	1.00	1.0756	266.8	246.76	47 633.	10 073.	1.009	0.652	0.508	0.518
3.0	5.00	1.0264	158.3	290.80	32 425.	11 396.	1.009	0.652	0.509	0.534

Table B.2. continued.

$M_p (M_J)$	Age (Gyr)	$R_{0,p} (R_J)$	$T_{\text{eff}} (K)$	$P_c (\text{M Bar})$	$T_c (K)$	$\rho_c (\text{kg/m}^3)$	$n$	$\kappa_n$	$k_2$	
									Analytic	Numeric
5.0	0.05	1.2306	746.7	437.22	134 158.	12 207.	1.038	0.643	0.491	0.477
5.0	0.10	1.1855	620.1	509.10	121 231.	13 722.	1.053	0.638	0.483	0.479
5.0	0.50	1.1058	401.2	671.34	92 480.	16 920.	1.076	0.631	0.469	0.485
5.0	1.00	1.0775	333.8	741.09	80 859.	18 218.	1.081	0.630	0.467	0.489
5.0	5.00	1.0226	214.3	900.43	54 736.	21 064.	1.085	0.629	0.464	0.498
8.0	0.05	1.2338	986.7	1202.57	222 136.	20 971.	1.140	0.612	0.434	0.453
8.0	0.10	1.1759	804.3	1468.06	201 343.	24 340.	1.159	0.607	0.425	0.452
8.0	0.50	1.0854	516.0	2028.59	154 227.	30 946.	1.178	0.601	0.415	0.452
8.0	1.00	1.0568	428.1	2248.11	135 487.	33 390.	1.179	0.601	0.414	0.454
8.0	5.00	1.0018	278.2	2740.70	94 044.	38 622.	1.175	0.602	0.416	0.461
10.0	0.05	1.2355	1131.0	1940.74	286 246.	27 042.	1.191	0.598	0.408	0.439
10.0	0.10	1.1682	924.2	2439.07	259 634.	32 036.	1.206	0.593	0.401	0.438
10.0	0.50	1.0703	582.7	3458.94	198 170.	41 464.	1.217	0.590	0.395	0.437
10.0	1.00	1.0415	482.5	3839.83	174 150.	44 787.	1.215	0.591	0.396	0.439
10.0	5.00	0.9873	313.6	4676.54	121 844.	51 786.	1.206	0.593	0.400	0.445
13.0	0.05	1.2413	1330.1	3355.37	388 856.	35 933.	1.243	0.583	0.383	0.422
13.0	0.10	1.1605	1099.6	4390.75	352 475.	43 831.	1.249	0.581	0.379	0.421
13.0	0.50	1.0501	684.2	6502.34	268 237.	58 583.	1.247	0.581	0.380	0.422
13.0	1.00	1.0203	559.1	7258.53	234 464.	63 563.	1.243	0.583	0.383	0.423
13.0	5.00	0.9677	361.2	8837.13	166 014.	73 551.	1.231	0.586	0.388	0.429
17.0	0.05	1.5180	1963.5	2728.85	566 417.	27 110.	1.258	0.578	0.375	0.403
17.0	0.10	1.2104	1460.9	6602.33	518 481.	52 312.	1.287	0.570	0.362	0.405
17.0	0.50	1.0308	829.1	12 389.70	373 005.	83 468.	1.270	0.575	0.370	0.408
17.0	1.00	0.9989	672.8	13 988.06	325 053.	91 373.	1.264	0.577	0.373	0.410
17.0	5.00	0.9441	421.3	17 311.92	230 449.	107 176.	1.253	0.580	0.378	0.415
20.0	0.05	1.3776	1899.6	5422.33	663 050.	42 143.	1.301	0.566	0.356	0.396
20.0	0.10	1.1891	1528.5	9683.22	607 482.	64 873.	1.303	0.566	0.355	0.397
20.0	0.50	1.0200	903.9	17 617.27	446 001.	101 492.	1.281	0.572	0.365	0.401
20.0	1.00	0.9827	731.4	20 350.09	387 102.	113 070.	1.275	0.574	0.368	0.403
20.0	5.00	0.9291	458.3	25 212.93	276 207.	132 824.	1.265	0.576	0.372	0.407
25.	0.05	1.5200	2127.	5 955.	815 455.	40 447.	1.287	0.570	0.362	0.395
25.	0.10	1.2578	1787.	12 709.	795 339.	71 202.	1.304	0.565	0.354	0.396
25.	0.50	1.0257	1044.	28 841.	590 541.	131 050.	1.305	0.565	0.354	0.389
25.	1.00	0.9800	837.	34 513.	512 744.	149 997.	1.300	0.566	0.356	0.390
25.	5.00	0.9131	521.	45 516.	364 680.	184 780.	1.293	0.568	0.359	0.393
30.	0.05	1.4417	2251.	10 697.	1031 299.	57 276.	1.302	0.566	0.355	0.395
30.	0.10	1.2210	1942.	21 054.	1009 122.	94 918.	1.324	0.560	0.346	0.386
30.	0.50	1.0186	1178.	44 101.	755 593.	164 995.	1.324	0.560	0.345	0.379
30.	1.00	0.9639	951.	55 015.	657 633.	194 894.	1.321	0.560	0.347	0.380
30.	5.00	0.8894	587.	75 828.	465 898.	248 448.	1.319	0.561	0.347	0.382
35.	0.05	1.4087	2355.	16 000.	1248 903.	71 920.	1.315	0.562	0.349	0.391
35.	0.10	1.2392	2087.	27 668.	1218 128.	108 155.	1.342	0.555	0.338	0.375
35.	0.50	1.0140	1338.	62 590.	941 772.	199 702.	1.344	0.554	0.337	0.371
35.	1.00	0.9501	1089.	81 296.	823 309.	243 366.	1.343	0.554	0.337	0.371
35.	5.00	0.8678	653.	117 258.	573 154.	321 847.	1.346	0.554	0.336	0.372
40.	0.05	1.4201	2460.	20 626.	1456 790.	81 371.	1.331	0.558	0.342	0.384
40.	0.10	1.2789	2220.	32 737.	1421 580.	114 919.	1.359	0.550	0.330	0.365
40.	0.50	1.0115	1477.	84 607.	1156 557.	234 911.	1.362	0.549	0.329	0.363
40.	1.00	0.9389	1211.	114 372.	1016 621.	295 137.	1.364	0.548	0.328	0.363
40.	5.00	0.8479	721.	173 644.	687 696.	406 412.	1.372	0.546	0.325	0.363
45.	0.05	1.4571	2550.	23 906.	1644 054.	85 812.	1.344	0.554	0.337	0.378
45.	0.10	1.3266	2341.	36 613.	1617 554.	118 015.	1.373	0.546	0.325	0.357
45.	0.50	1.0104	1587.	109 823.	1394 789.	269 944.	1.379	0.544	0.322	0.356
45.	1.00	0.9293	1312.	154 381.	1233 338.	349 384.	1.384	0.543	0.320	0.356
45.	5.00	0.8296	797.	246 867.	810 090.	500 992.	1.397	0.539	0.314	0.355
50.	0.05	1.5084	2624.	26 059.	1812 465.	86 914.	1.353	0.552	0.333	0.372
50.	0.10	1.3661	2443.	40 788.	1816 290.	121 580.	1.382	0.544	0.321	0.352
50.	0.50	1.0105	1696.	137 864.	1657 050.	304 354.	1.394	0.540	0.316	0.350
50.	1.00	0.9212	1416.	201 021.	1473 950.	405 043.	1.401	0.538	0.313	0.350
50.	5.00	0.8133	877.	337 922.	939 025.	603 700.	1.420	0.533	0.305	0.347



Table B.2. continued.

$M_p (M_J)$	Age (Gyr)	$R_{0,p} (R_J)$	$T_{\text{eff}} (K)$	$P_c$ (MBar)	$T_c (K)$	$\rho_c$ (kg/m <sup>3</sup> )	$n$	$\kappa_n$	$k_2$	
									Analytic	Numeric
55.	0.05	1.5706	2692.	27 233.	1961 060.	85 721.	1.362	0.549	0.329	0.366
55.	0.10	1.4046	2529.	44 642.	2 009 304.	124 155.	1.389	0.542	0.318	0.348
55.	0.50	1.0124	1807.	168 106.	1939 776.	336 623.	1.406	0.537	0.311	0.346
55.	1.00	0.9152	1523.	254 050.	1737 899.	460 099.	1.415	0.535	0.307	0.344
55.	5.00	0.7992	961.	449 023.	1078 605.	712 565.	1.440	0.528	0.297	0.340
60.	0.05	1.6344	2755.	28 052.	2098 173.	84 004.	1.371	0.547	0.325	0.361
60.	0.10	1.4394	2605.	48 560.	2198 748.	126 745.	1.394	0.540	0.316	0.345
60.	0.50	1.0028	2022.	210 699.	2180 116.	384 420.	1.412	0.535	0.308	0.342
60.	1.00	0.9044	1686.	322 274.	1968 043.	528 985.	1.427	0.531	0.303	0.340
60.	5.00	0.7871	1046.	576 706.	1239 622.	823 831.	1.455	0.524	0.291	0.334
65.	0.05	1.7083	2808.	28 001.	2215 973.	80 685.	1.379	0.544	0.322	0.356
65.	0.10	1.4891	2670.	50 342.	2363 839.	125 232.	1.400	0.538	0.313	0.341
65.	0.50	1.0113	2143.	242 171.	2453 178.	410 782.	1.421	0.533	0.305	0.339
65.	1.00	0.9040	1835.	384 628.	2244 926.	581 941.	1.438	0.528	0.298	0.336
65.	5.00	0.7792	1144.	713 179.	1456 962.	926 551.	1.465	0.521	0.288	0.330
70.	0.05	1.9273	2830.	21 154.	2211 446.	62 872.	1.407	0.537	0.310	0.334
70.	0.10	1.5424	2723.	51 330.	2516 482.	122 503.	1.407	0.537	0.310	0.337
70.	0.50	1.0258	2247.	267 457.	2738 379.	426 572.	1.426	0.531	0.303	0.336
70.	1.00	0.9137	1966.	430 915.	2558 262.	610 607.	1.443	0.527	0.296	0.332
70.	5.00	0.7785	1275.	830 427.	1812 842.	996 941.	1.466	0.521	0.287	0.328
75.	0.05	1.9854	2855.	21 758.	2324 345.	62 117.	1.415	0.534	0.307	0.332
75.	0.10	1.5863	2769.	53 086.	2670 747.	121 465.	1.412	0.535	0.309	0.334
75.	0.50	1.0459	2352.	285 273.	3027 221.	432 191.	1.427	0.531	0.302	0.334
75.	1.00	0.9304	2108.	461 523.	2903 894.	620 803.	1.443	0.527	0.296	0.331
75.	5.00	0.7962	1527.	873 708.	2288 897.	998 714.	1.466	0.521	0.287	0.326

**Notes.** For each planetary mass ( $M_p$ ) and age, this table gives the spherical equilibrium radius ( $R_{0,p}$ ,  $R_J \equiv 7.1492 \times 10^7$  m), the effective temperature ( $T_{\text{eff}}$ ), the central pressure ( $P_c$ ), temperature ( $T_c$ ) and density ( $\rho_c$ ) along with the polytropic index ( $n$ ), the dimensionless moment of inertia ( $\kappa_n$ , see Eq. (30)) and Love number ( $k_2$ ).  $k_2$  was derived both with our analytical formula (Eq. (42); analytic) and with a numerical method (see Appendix A; numeric).

**Table B.3.** Same as Table B.2, for the most irradiated planets ( $F_{\star} = 4.18 \times 10^6 \text{ W m}^{-2}$ ).

$M_p (M_J)$	Age (Gyr)	$R_{0,p} (R_J)$	$T_{\text{eff}} (K)$	$P_c$ (MBar)	$T_c (K)$	$\rho_c$ (kg/m <sup>3</sup> )	$n$	$\kappa_n$	$k_2$	
									Analytic	Numeric
0.5	0.05	1.4802	261.9	3.86	26 591.	1109.	1.243	0.583	0.383	0.253
0.5	0.10	1.3812	219.0	4.33	24 369.	1195.	1.129	0.616	0.441	0.296
0.5	0.50	1.2323	143.8	5.38	20 269.	1385.	0.975	0.662	0.529	0.375
0.5	1.00	1.1885	118.8	5.81	18 784.	1459.	0.935	0.674	0.554	0.402
0.5	5.00	1.1115	76.8	6.79	15 221.	1626.	0.872	0.693	0.595	0.450
0.6	0.05	1.4449	287.5	5.53	30 336.	1332.	1.257	0.579	0.376	0.268
0.6	0.10	1.3561	242.5	6.16	27 836.	1438.	1.156	0.608	0.426	0.310
0.6	0.50	1.2202	155.5	7.47	22 690.	1636.	1.001	0.654	0.513	0.391
0.6	1.00	1.1808	128.1	8.02	20 870.	1723.	0.964	0.665	0.536	0.416
0.6	5.00	1.1100	81.7	9.27	17 153.	1904.	0.904	0.683	0.574	0.462
0.7	0.05	1.4167	313.4	7.68	34 787.	1542.	1.258	0.578	0.375	0.281
0.7	0.10	1.3347	263.3	8.61	31 797.	1689.	1.173	0.603	0.417	0.322
0.7	0.50	1.2099	166.9	10.31	25 479.	1938.	1.028	0.646	0.497	0.403
0.7	1.00	1.1734	137.1	11.03	23 351.	2028.	0.993	0.656	0.518	0.427
0.7	5.00	1.1083	87.1	12.62	19 183.	2231.	0.936	0.674	0.553	0.471
0.8	0.05	1.3997	335.1	9.86	38 796.	1706.	1.234	0.585	0.387	0.295
0.8	0.10	1.3207	280.5	11.21	35 538.	1893.	1.169	0.604	0.419	0.334
0.8	0.50	1.2015	177.1	13.69	28 328.	2228.	1.049	0.639	0.485	0.411
0.8	1.00	1.1680	145.0	14.52	25 811.	2319.	1.015	0.650	0.505	0.434
0.8	5.00	1.1064	91.9	16.56	21 024.	2555.	0.962	0.666	0.537	0.476
0.9	0.05	1.3902	354.1	12.10	42 282.	1859.	1.195	0.596	0.406	0.309
0.9	0.10	1.3123	295.9	13.92	38 890.	2074.	1.149	0.610	0.430	0.346
0.9	0.50	1.1955	186.6	17.37	31 105.	2479.	1.059	0.636	0.479	0.417
0.9	1.00	1.1642	152.2	18.43	28 174.	2599.	1.028	0.646	0.497	0.439
0.9	5.00	1.1048	96.5	21.02	22 830.	2866.	0.981	0.660	0.525	0.479
1.0	0.05	1.3845	372.0	14.45	45 609.	2005.	1.155	0.608	0.427	0.322
1.0	0.10	1.3074	310.6	16.76	42 025.	2248.	1.124	0.617	0.443	0.357
1.0	0.50	1.1918	195.7	21.29	33 727.	2719.	1.060	0.636	0.478	0.424
1.0	1.00	1.1616	159.4	22.69	30 526.	2863.	1.035	0.644	0.493	0.445
1.0	5.00	1.1038	100.7	25.92	24 599.	3168.	0.994	0.656	0.517	0.482
1.2	0.05	1.3802	403.7	19.45	51 893.	2287.	1.082	0.630	0.466	0.347
1.2	0.10	1.3038	337.8	22.81	47 931.	2582.	1.070	0.633	0.473	0.379
1.2	0.50	1.1886	213.2	29.76	38 662.	3176.	1.048	0.640	0.485	0.437
1.2	1.00	1.1592	173.3	31.97	35 060.	3362.	1.034	0.644	0.494	0.454
1.2	5.00	1.1032	108.7	36.81	28 050.	3754.	1.007	0.652	0.510	0.487
1.5	0.05	1.3816	441.7	28.32	59 797.	2739.	1.010	0.651	0.508	0.375
1.5	0.10	1.3063	371.5	33.41	55 635.	3094.	1.009	0.652	0.508	0.403
1.5	0.50	1.1899	236.2	44.60	45 509.	3844.	1.017	0.649	0.503	0.453
1.5	1.00	1.1602	191.8	48.41	41 202.	4100.	1.016	0.649	0.504	0.466
1.5	5.00	1.1047	119.5	56.43	32 981.	4612.	1.005	0.653	0.511	0.494
1.8	0.05	1.3842	476.2	39.02	67 811.	3207.	0.976	0.662	0.528	0.394
1.8	0.10	1.3099	401.5	46.16	62 943.	3636.	0.976	0.661	0.528	0.421
1.8	0.50	1.1931	257.0	62.12	51 794.	4534.	0.993	0.656	0.518	0.464
1.8	1.00	1.1625	208.6	67.92	47 144.	4853.	1.000	0.654	0.514	0.476
1.8	5.00	1.1068	129.5	79.87	37 666.	5492.	0.999	0.655	0.514	0.499
2.1	0.05	1.3877	507.3	51.29	77 544.	3643.	0.963	0.665	0.536	0.408
2.1	0.10	1.3137	429.3	61.02	71 611.	4159.	0.964	0.665	0.536	0.432
2.1	0.50	1.1963	276.7	82.88	58 167.	5246.	0.980	0.660	0.526	0.472
2.1	1.00	1.1650	224.2	90.91	53 093.	5622.	0.990	0.657	0.520	0.482
2.1	5.00	1.1087	138.8	107.73	42 307.	6398.	0.996	0.656	0.516	0.502
3.0	0.05	1.3997	583.5	96.63	106 857.	4903.	0.960	0.666	0.538	0.435
3.0	0.10	1.3263	499.2	116.54	99 725.	5658.	0.964	0.665	0.536	0.453
3.0	0.50	1.2058	329.1	164.27	80 267.	7377.	0.983	0.659	0.524	0.480
3.0	1.00	1.1709	267.7	183.21	72 047.	8026.	0.993	0.657	0.518	0.488
3.0	5.00	1.1108	163.4	222.49	56 621.	9310.	1.006	0.653	0.510	0.501

Table B.3. continued.

$M_p (M_J)$	Age (Gyr)	$R_{0,p} (R_J)$	$T_{\text{eff}} (K)$	$P_c$ (MBar)	$T_c (K)$	$\rho_c$ (kg/m <sup>3</sup> )	$n$	$\kappa_n$	$k_2$	
									Analytic	Numeric
5.0	0.05	1.4224	741.1	247.80	166 910.	7870.	0.997	0.655	0.515	0.457
5.0	0.10	1.3473	619.5	304.77	157 781.	9229.	1.007	0.652	0.509	0.466
5.0	0.50	1.2133	419.3	464.43	128 666.	12 786.	1.044	0.641	0.488	0.476
5.0	1.00	1.1708	344.7	537.24	115 271.	14 293.	1.059	0.637	0.479	0.478
5.0	5.00	1.1014	213.8	684.92	90 171.	17 174.	1.077	0.631	0.469	0.483
8.0	0.05	1.4420	932.1	636.38	259 574.	12 943.	1.086	0.628	0.464	0.449
8.0	0.10	1.3495	793.0	831.43	248 326.	15 866.	1.105	0.623	0.453	0.453
8.0	0.50	1.2051	525.5	1327.72	212 307.	22 576.	1.149	0.610	0.430	0.453
8.0	1.00	1.1571	445.5	1570.48	192 724.	25 593.	1.164	0.605	0.422	0.451
8.0	5.00	1.0748	278.7	2111.44	147 177.	31 873.	1.179	0.601	0.414	0.452
10.0	0.05	1.4483	1051.8	1016.77	325 164.	16 633.	1.143	0.612	0.433	0.438
10.0	0.10	1.3480	893.7	1359.72	313 318.	20 717.	1.163	0.606	0.422	0.440
10.0	0.50	1.1931	588.7	2240.54	270 490.	30 079.	1.200	0.595	0.403	0.438
10.0	1.00	1.1450	500.6	2647.31	247 482.	34 031.	1.210	0.592	0.399	0.437
10.0	5.00	1.0583	321.2	3616.15	188 199.	42 848.	1.217	0.590	0.395	0.437
13.0	0.05	1.4543	1227.3	1771.70	427 626.	22 312.	1.207	0.593	0.400	0.422
13.0	0.10	1.3420	1036.9	2453.77	414 870.	28 462.	1.228	0.587	0.390	0.422
13.0	0.50	1.1746	684.1	4190.16	360 362.	42 333.	1.249	0.581	0.380	0.421
13.0	1.00	1.1260	572.1	4952.80	331 095.	47 900.	1.251	0.580	0.379	0.421
13.0	5.00	1.0376	378.2	6812.26	253 286.	60 644.	1.245	0.582	0.381	0.422
17.0	0.05	1.9236	1814.9	1092.21	530 529.	13 540.	1.206	0.593	0.401	0.392
17.0	0.10	1.5737	1547.6	2343.85	565 858.	24 210.	1.250	0.581	0.379	0.402
17.0	0.50	1.1635	839.0	7729.08	492 879.	58 757.	1.285	0.571	0.363	0.405
17.0	1.00	1.1059	676.3	9432.93	451 135.	68 127.	1.280	0.572	0.365	0.406
17.0	5.00	1.0153	451.7	13 139.79	350 018.	87 181.	1.267	0.576	0.371	0.409
20.0	0.05	1.7413	1796.7	2127.33	643 444.	20 955.	1.257	0.579	0.376	0.392
20.0	0.10	1.4005	1444.2	5080.99	666 543.	40 165.	1.300	0.566	0.356	0.395
20.0	0.50	1.1447	901.3	11 241.96	577 707.	72 520.	1.299	0.567	0.357	0.398
20.0	1.00	1.0891	731.1	13 657.81	530 282.	83 878.	1.292	0.569	0.360	0.399
20.0	5.00	1.0015	492.3	18 915.42	418 729.	106 994.	1.277	0.573	0.366	0.402